Quarterly Report for

April - June 2000

Stanford Geothermal Program

DE-FG07-99ID13763

Table of Contents

1. MEASUREMENTS OF STEAM-WATER RELATIVE PERMEABILITY

This research project is being conducted by Research Assistant Peter O'Connor and Professor Roland Horne. The aim is to measure relative permeability relations for steam and water flowing simultaneously in rock and to examine the effects of temperature, flow rate, and rock type. In the first stage, the experiments will attempt to reproduce results obtained in a previous experiment (Mahiya, 1999), but holding the experimental pressure as close as possible to a constant value.

1.1 BACKGROUND

An X-ray CT technique has been used in recent years to measure the distribution of steam and water saturation in rocks to obtain steam-water relative permeability curves (Satik and Horne, 1998, Mahiya, 1999).

The current experiment is attempting to maintain a constant pressure, to avoid complications of the slip factor and also to maintain a constant temperature. As the experiment will be constantly at an inlet gauge pressure of 15 psi, it will necessarily be at a constant 120ºC at the inlet in order to have two-phase flow throughout, with the rest of the core being at the saturation temperature for the pressure at that point. Our expectation is an identical pressure profile and temperature profile for every step of the process.

1.2 EXPERIMENTAL PROCEDURE

A Berea sandstone was drained, flushed with nitrogen, then subjected to a vacuum. A dry X-ray scan was made to obtain CT_{dry}. The next step was to saturate the core with water and scan to obtain CT_{wet}; however, the CT scanner failed at this point and this step will be repeated next quarter. From these scans, a porosity distribution will be obtained, expected to yield an average value of 24.7%. In the next step, hot liquid water is flowed through to obtain CT_{hw}, which is necessary to calculate experimental saturations. The next steps are the actual flow-through experiments. The core will be under a pressure gradient of approximately 15 psi across the 41-cm length. First, the core is saturated with steam. Steam flow rate will be gradually lowered in 10% increments, to implement an imbibition process whereby the wetting phase (water) displaces the nonwetting phase (steam). A flexible heat guard ensures negligible overall heat loss for a near-adiabatic process. The flexible heat guard control mechanism was redesigned this year. At each step, the system will reach a steady state and will then be subject to CT scan to measure saturation. Steam flow rate will be reduced to 0%, then increased. This second sequence will be a drainage sequence.

At every stage, pressure, temperature and heat fluxes from the core are to be measured. Calculated relative permeability to steam and water are then plotted against the saturation measurements. The major suggested change from the previous experiment is to perform the imbibition step first. Performing the imbibition step first allows determination of the maximum pressure. This pressure can be maintained by increasing flow rates if necessary.

In the current quarter, we worked to determine the correct flow rates and power inputs to ensure a pressure differential of 15 psi and a temperature at the inlet of slightly over 120ºC for the steam, and slightly under 120ºC for the hot water. In this procedure, we determined several pairs of flow rates for water and steam, at different ratios, to result in steady-state flow with a pressure differential of 15 psi. This process also determined the corresponding voltage and current settings for the hot water and steam heaters and for the flexible heater. All that is unknown is the saturation; once the CT scanner is available, it should be a simple matter to determine the saturation. However, the core was damaged through excessive heat in the process. The current activity involves repairing the core and checking to see if any aspects of the apparatus have been altered significantly. For example, a change in system permeability or heat transfer coefficient could have a significant effect on the experiment. If the previously established flow settings still produce a 15-psi differential and two-phase flow, then the project will be continued from where we left off. Otherwise, we will adjust flow settings to fit the new system parameters, or construct a new core holder if necessary.

1.3 FUTURE RESEARCH

Future research will involve repeating the experiment at different pressure gradients and temperatures. The next experiment will probably occur at approximately half the current pressure gradient. In each case, the experiment will maintain a uniform pressure gradient for the range of saturations.

Also under consideration is the possibility of using acoustic sounding to determine saturation. While not as precise as the CT scanner, this method has the advantage of producing average saturation readings extremely quickly.

2. AN EXPERIMENTAL INVESTIGATION OF BOILING HEAT CONVECTION WITH RADIAL FLOW IN A FRACTURE

This project has been conducted by Research Assistant Robb Barnitt and Professor Roland Horne. The goal has been to investigate and compare the heat flux and temperature gradients that develop during boiling with liquid injection into a simulated rock fracture. Another objective was to develop a boiling convection coefficient for use in calculating heat transfer with boiling in fractured geothermal rock. Improved understanding and modeling of heat transfer in a fracture will lead ultimately to better strategies for injection into fractured geothermal reservoirs. The project was completed during the quarter, and a technical report of the results has been prepared.

2.1 INTRODUCTION

The focus of this work has been the coupling of conductive heat transfer and boiling convective heat transfer, with boiling flow in a rock fracture. A series of experiments observed differences in boiling regimes and behavior, and attempted to quantify a boiling convection coefficient. The experimental study involved boiling radial flow in a simulated fracture, bounded by a variety of materials. Nonporous and impermeable aluminum, highly porous and permeable Berea sandstone, and minimally porous and permeable graywacke from The Geysers geothermal field. On nonporous surfaces, the heat flux was not coupled strongly to injection rate into the fracture. However, for porous surfaces, heat flux, and associated values of excess temperature and a boiling convection coefficient exhibited variation with injection rate. Nucleation was shown to occur not upon the visible surface of porous materials, but a distance below the surface, within the matrix. The depth of boiling was a function of injection rate, thermal power supplied to the fracture, and the porosity and permeability of the rock. Although matrix boiling beyond the fracture wall may apply only to a finite radius around the point of injection, higher values of heat flux and a boiling convection coefficient may be realized with boiling in a porous, rather than nonporous surface bounded fracture.

2.2 DATA COMPARISON OVER RANGE OF MATERIALS

When evaporation occurs at a solid-liquid interface, it is identified as boiling. Boiling begins when the temperature of the surface (T_{surf}) exceeds the saturation temperature (T_{sat}) corresponding to the liquid pressure. Thermal energy transferred from the solid surface to the liquid drives the process. The form of Newton's Law of Cooling that describes this mode of heat transfer and quantifies the heat flux (q'') is given by Equation 2.1.

$$q'' = h(T_{surf} - T_{sat}) = hT_e \tag{2.1}$$

Measured data and calculated values for heat flow rate q'', excess temperature T_e, and heat transfer coefficient h can be compared for each of the three experimental materials employed. Because only one power input was used in the sandstone experiment, data collected for approximately the same power input for the aluminum and graywacke experiments were used for comparison.

2.2.1 Heat Flux Comparison

Although heat flux is not strongly coupled to injection rate for boiling on a confined nonporous surface, it is coupled for confined boiling on the two porous surfaces (Figure 2.1).

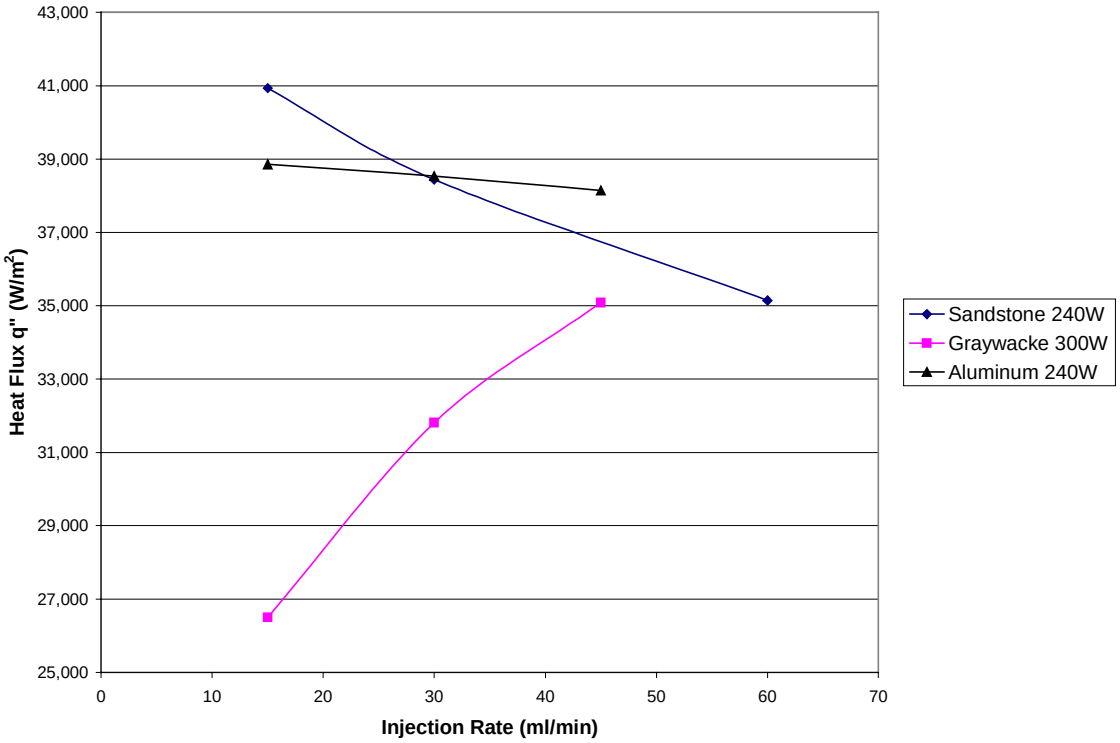

Figure 2.1: Heat flux comparison.

Due to asperity-induced nucleation sites on the porous surfaces, higher heat fluxes would be expected than for equal powers and injection rates on a nonporous surface. A higher heat flux for sandstone at 15 ml/min is observed than for aluminum at 15 ml/min. However, for higher injection rates, the sandstone heat flux drops below the relatively constant heat flux value. This may indicate the presence of a vapor blanket, in which lower thermal conductivity vapor reduces the heat flux.

Given smaller pores and asperities present in graywacke, heat fluxes slightly higher than those observed in the sandstone would be expected. However, this was not observed. The 15 ml/min injection rate corresponded with superheated conditions and the absence of boiling in the graywacke matrix. The heat flux increased sharply with higher injection rates, and as boiling began in the matrix.

2.2.2 Excess Temperature Comparison

Although T_e is not strongly coupled to injection rate for boiling on a confined nonporous surface, it is coupled for confined boiling on the two porous surfaces (Figure 2.2). T_e increases slightly with increasing injection rate for sandstone. A decreasing value of T_{sat} drives this trend. This subcooled boiling condition is also evident in the increasing T_e trend for graywacke. The lower permeability of the graywacke likely led to increased injectate retention in the fracture, and consequently lowered the value of T_{sat}.

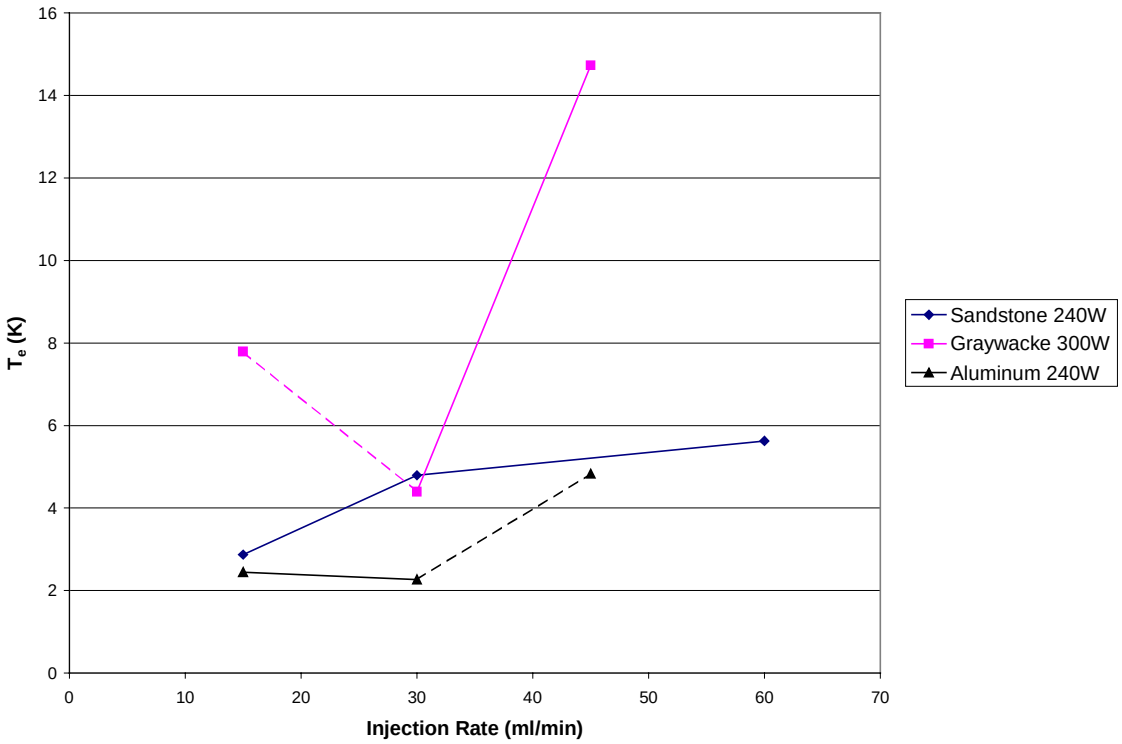

Figure 2.2: Excess temperature comparison.

2.2.3 Boiling Convection Coefficient Comparison

Although the h is not strongly coupled to injection rate for boiling on a confined nonporous surface, it is coupled for confined boiling on the two porous surfaces (Figure 2.3). The decreasing trend for sandstone is driven mainly by the decrease in heat flux with increasing injection rate. Although the q'' and T_e trends for graywacke were increasing, the resultant trend is decreasing with increasing injection rate. A maximum for q'' may not correspond with a maximum h for boiling on graywacke.

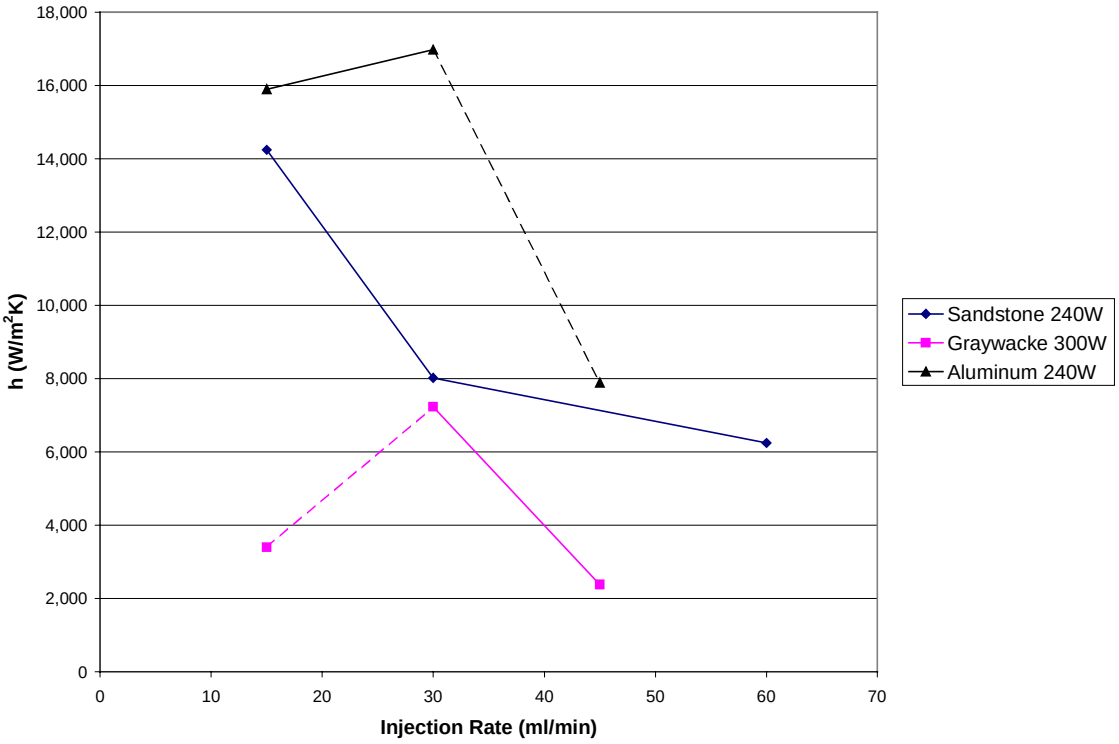

Figure 2.3: Boiling convection coefficient comparison.

2.3 DEPTH OF BOILING IN POROUS MATERIALS

Our results indicated differences in boiling depth for varying injection rates, power inputs, and materials. Figure 2.4 illustrates these differences. Calculated values from superheated conditions are not plotted.

Due to the higher porosity and permeability of the sandstone, injected water is able to penetrate deeper into the matrix before boiling. The larger pores in sandstone may slightly affect the boiling depth, as nucleation will not occur as rapidly (i.e. at a shallower matrix depth) as in the smaller pored graywacke.

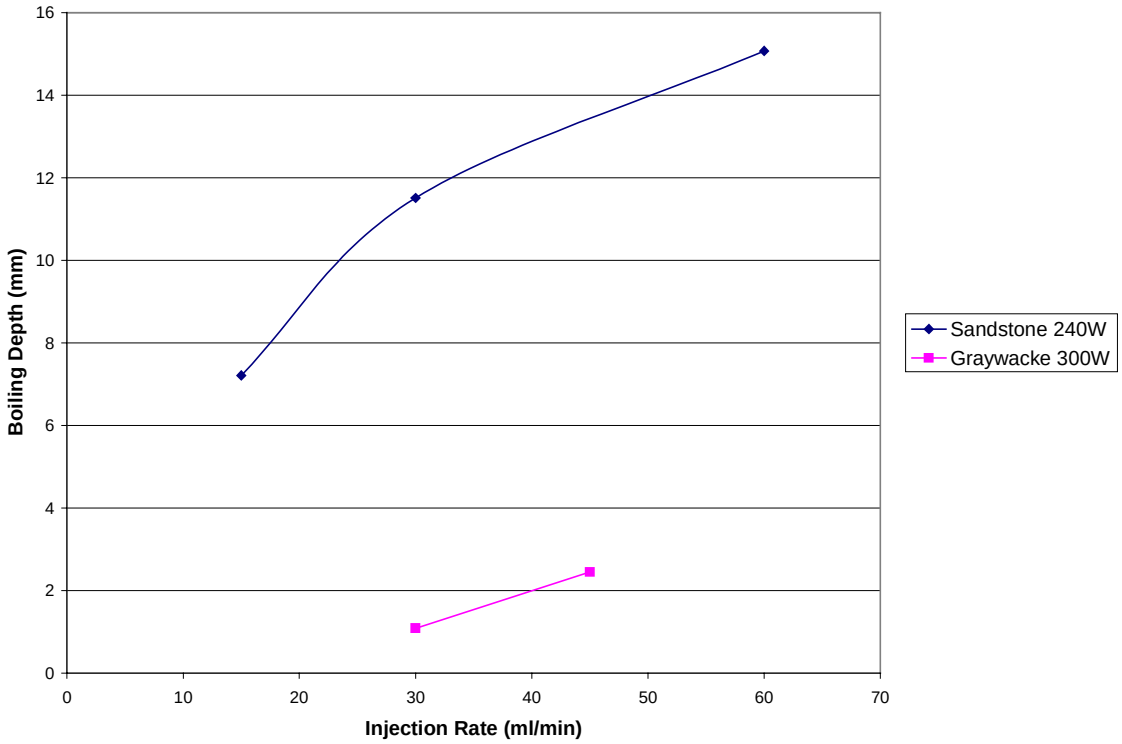

Figure 2.4: Boiling depth variation with injection rate and material.

2.4 APPLICATION OF RESULTS

Experimental analysis of boiling on a confined, nonporous surface indicated that heat flux was not coupled to injection rate into the simulated fracture. However, injection rate was observed to influence the heat flux with boiling on a confined, porous surface. Visual observations during the experiments indicated that injected fluid penetrated the porous matrix close to the injection point. The fluid penetrated the matrix to a depth at which saturated conditions existed, before flowing radially to the edge of the experimental disk. It is likely that the boiling depth decreased with distance from the point of injection.

Experimental results also indicated that with increasing power supplied to the fracture, the vapor fraction increased, and boiling depth decreased. As indicated in the graywacke experiment, superheated conditions were attained at some low injection rates, resulting in boiling occurring only in the fracture, and not in the matrix.

Applying these two points to an injection scenario in a fractured geothermal field, it is likely that the magnitude of the injection rate may only affect a finite region close to the point of injection. Boiling may occur in the matrix in this region, but as injected fluid travels along a given fracture, the boiling depth would decrease until superheated conditions applied. At this point, the conventional pool-boiling relationship given in

Equation 2.1 is appropriate. However, onset of nucleation and therefore the magnitude of the heat flux and boiling convection coefficient are functions of pore size. Although it may be appropriate to model the boiling convection coefficient using the relationship and definitions given in Equation 2.1, another correlation may be required to account for the advanced pore- and asperity-induced nucleation effects. It is worthy of note that heat fluxes for graywacke increased with increasing injection rate. This was not observed for either nonporous aluminum or highly porous sandstone, in which a vapor blanket may have formed within the matrix. Further research would be appropriate in this area.

3. INFERRING IN-SITU AND IMMOBILE WATER SATURATIONS FROM FIELD MEASUREMENTS

This project has been conducted by Research Assistant Rodolfo Belen Jr., Research Associate Kewen Li, and Prof. Roland Horne. The aim was to infer the endpoint saturation of steam and liquid water relative permeability curves of geothermal reservoir rocks as well as the in-situ water saturation of geothermal reservoirs from laboratory and field measurements. The project was completed during the quarter, and a technical report and scientific paper were prepared describing the results.

3.1 SUMMARY

This study developed models of vapor and liquid geothermal reservoirs, based on Darcy's law and material and energy conservation equations. These models can be used as tools to infer the in-situ and immobile water saturations from field measurements of cumulative mass production, discharge enthalpy and temperature. The knowledge of the in-situ and immobile water saturations is valuable in evaluating geothermal reservoir performance.

Knowing rock and fluid properties, and the difference between the stable initial, T_o, and dry-out, T_d, downhole temperatures, the in-situ and immobile water saturations of vapor-dominated reservoirs can be estimated. On the other hand, the in-situ and immobile water saturation, and the change in mobile water content of liquid-dominated reservoirs can be inferred from data of the cumulative mass production, Δm, and enthalpy, h'.

Comparison with two-phase radial flow simulation results confirmed the validity and usefulness of these models.

3.2 INTRODUCTION

The discharge of saturated or superheated steam during the exploitation of vapor-dominated geothermal reservoirs greatly exceeds what can be stored as vapor. Therefore, vapor-dominated reservoirs must contain substantial amounts of liquid water to sustain production (James, 1968; Nathenson 1975; Grant, 1979). In describing the response of vapor-dominated reservoirs to exploitation, it is valid to assume that the liquid water is completely immobile. Although water may be slightly mobile in the natural state of the reservoir, it is soon immobile because the water saturation drops as fluids are produced (Grant, 1979). The liquid water is adsorbed in the pores of the reservoir matrix and is able to vaporize, but is not able to flow as liquid water.

Grant (1979) estimated the in-place water saturation of the Kawah Kamojang geothermal field, Java, based on variations in the gas content of the production fluids. Changing the flow rate at the wellhead produces a response in the reservoir pressure and gas content, which allows for the estimation of the in-place water saturation. In contrast, this study aims to infer the in-situ and immobile water saturations from field measurements of changes in the flowing enthalpies of producing wells as well as downhole wellbore temperatures.

Zero-dimensional models can be used to describe the pressure, temperature and saturation profiles accompanying production. This study developed models of both vapor and liquid dominated geothermal reservoirs that can be used to infer the in-situ and immobile water saturation from field measurements of cumulative mass production, enthalpy and temperature.

3.3 ZERO-DIMENSIONAL MODELS

Darcy's law and the differential material and energy conservation equations that describe the response of geothermal reservoirs to exploitation can be combined to form simple zero-dimensional models. For the case of vapor dominated geothermal systems, the only mobile phase is steam. The flow of dry steam can be described by Equations 3.1 to 3.3. It is assumed that the immobile water does not impede the flow of steam and that the steam flow is governed by Darcy's law.

$$\phi \frac{\partial}{\partial t}\{s\rho_w + (1-s)\rho_s\} = -\nabla \cdot (\vec{u}_s \rho_s) \tag{3.1}$$

$$\frac{\partial}{\partial t}\{(1-\phi)\rho_r c_r T + \phi s \rho_w h_w + \phi(1-s)\rho_s h_s\} = -\nabla \cdot (\vec{u}_s \rho_s h_s) \tag{3.2}$$

$$\vec{u}_s = -\frac{k k_{rs}}{\mu_s} \nabla p \tag{3.3}$$

Under reservoir conditions, the enthalpy of saturated steam is nearly constant with temperature. This approximation results in a simplified relation between pressure and saturation at any point in the reservoir.

$$(1-\phi)\rho_r C_r T + \phi s \rho_w (h_w - h_s) = \text{constant} \tag{3.4}$$

Reduction in the reservoir pressure resulting from production is accompanied by a reduction in reservoir temperature to maintain saturation conditions. Heat must then be mined from the rock to cool it, which is achieved by vaporizing some of the liquid water to steam. Therefore, a decline in the reservoir pressure results in a decline in the reservoir liquid saturation. This mining of heat and consequent decline in liquid saturation continues as long as saturation conditions exist. The saturation falls to zero at dry out conditions and the in-place water saturation can then be estimated using the initial and dry out reservoir conditions (Grant 1979).

$$s_o = \frac{(1-\phi)}{\phi} \frac{\rho_r c_r (T_o - T_d)}{\rho_w (h_s - h_w)\big|_{T_o}} \tag{3.5}$$

This zero-dimensional model allows the calculation of the in-situ water saturation using rock and fluid properties and the initial, T_o, and dry-out, T_d, downhole or reservoir temperatures. In this case, the dry-out temperature is that temperature at which the reservoir has completely dried out and has started to produce superheated steam.

On the other hand, for the liquid dominated reservoir case, the differential material and energy balance equations (Equations 3.6 and 3.7) and the simplified equations describing the zero-dimensional model (Equations 3.8 and 3.9) are much more complicated because both water and steam phases are mobile.

$$\phi \frac{\partial}{\partial t}\{s\rho_w + (1-s)\rho_s\} = -\nabla \cdot (\vec{u}_w \rho_w + \vec{u}_s \rho_s) \quad (3.6)$$

$$\frac{\partial}{\partial t}\{(1-\phi)\rho_r c_r T + \phi s\rho_w h_w + \phi(1-s)\rho_s h_s\} = -\nabla \cdot (\vec{u}_w \rho_w h_w + \vec{u}_s \rho_s h_s) \quad (3.7)$$

$$\phi V\Delta(s\rho_w) + \phi V\Delta\{(1-s)\rho_s\} + m_w' + m_s' = 0 \quad (3.8)$$

$$\phi V\Delta(s\rho_w h_w) + \phi V\Delta\{(1-s)\rho_s h_s\} + (1-\phi)V\rho_r C_r \Delta T + m_w' h_w' + m_s' h_s' = 0 \quad (3.9)$$

The composition and enthalpy of the production fluids is determined by the mobility of steam and liquid water in the porous rock given by the relative permeabilities and viscosities of the two phases as shown in Equations 3.10 and 3.11.

$$m_w' = \frac{\rho_w \frac{k_{rw}}{\mu_w}}{\rho_w \frac{k_{rw}}{\mu_w} + \rho_s \frac{k_{rs}}{\mu_s}} \Delta m \quad (3.10)$$

$$m_s' = \frac{\rho_s \frac{k_{rs}}{\mu_s}}{\rho_w \frac{k_{rw}}{\mu_w} + \rho_s \frac{k_{rs}}{\mu_s}} \Delta m \quad (3.11)$$

3.4 SIMULATED TWO-PHASE RADIAL FLOW MODEL

The zero-dimensional models shown in the previous section assume that the pressures, temperatures and saturations are uniform throughout the reservoir. These models do not take into account the transient and spatial effects of two-phase flow in the reservoir. In order to investigate the validity and usefulness of these models in determining the in-situ and immobile saturations, two-phase radial flow was modeled using the reservoir simulator TOUGH2. The TOUGH2 simulation results were then compared with those predicted by the zero-dimensional models.

A cylindrical reservoir model was used in the TOUGH2 simulation runs. Reservoir radius is 1 kilometer and thickness is 10 meters. The model consists of 100 grid blocks and the grid size increases logarithmically from the center to the boundary of the reservoir. Initial reservoir temperature is 280°C. A single production well maintained at constant downhole wellbore pressure of 200 psia is located in the middle of the reservoir. Reservoir rock properties used in the simulation are those of Geysers geothermal rocks, which are listed in Table 3.1.

Table 3.1: Geysers geothermal rock properties.

Porosity	5%
Permeability	1 x 10^{-13} m^2
Rock density	2600 kg/m^3
Rock specific heat	485 J/kg°C

Figures 3.1 to 3.3 are semilog plots of the saturation, temperature and pressure profiles with time and radial distance from the well. Initially, water saturation throughout the reservoir in this particular simulation run is 0.3. As a response to production, reservoir pressure, temperature and saturation drop and boiling near the wellbore commences. The boiling front moves farther into the reservoir away from the well as two-phase steam is produced. However, water saturation stays above and never goes below the immobile water saturation. The reservoir eventually produces dry saturated steam. During this time, reservoir saturation has dropped below the immobile water saturation. Water remaining in the reservoir during this period is immobile water, which is able to vaporize but not able to flow.

At some point during production, the reservoir completely dries out and starts to produce superheated steam. Water saturation has dropped to zero throughout the reservoir. The sequence of events in the production history of the reservoir is labeled in Figure 3.1.

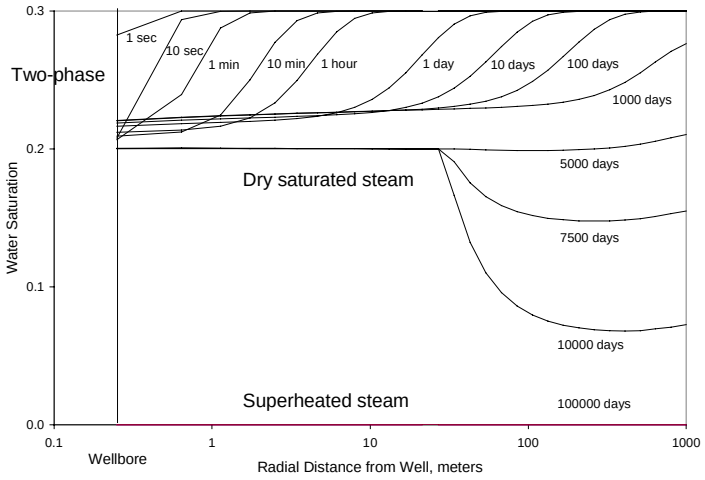

Figure 3.1: Water saturation profile with distance and time: s_{wi} = 0.3; s_{wr} = 0.2.

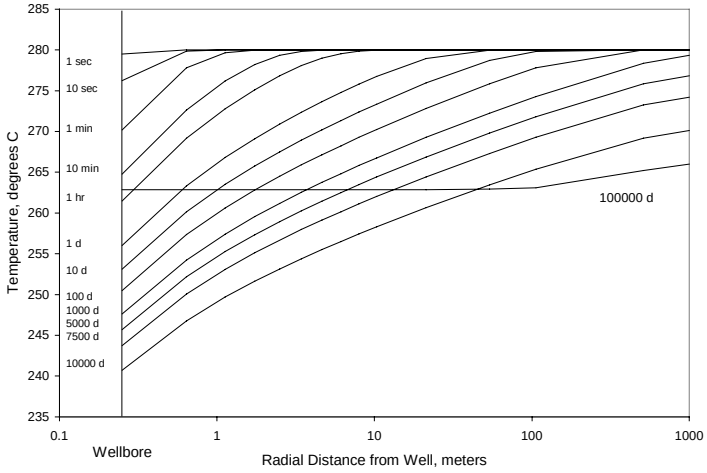

Figure 3.2: Temperature profile with distance and time: s_{wi} = 0.3; s_{wr} = 0.2.

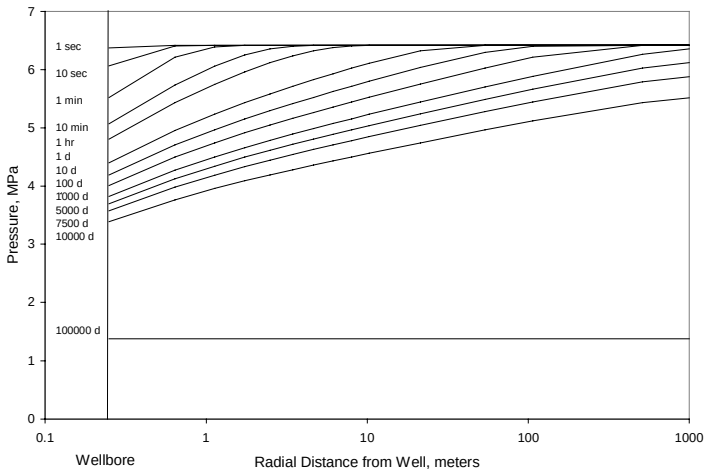

Figure3.3: Pressure profile with distance and time: s_{wi} = 0.3; s_{wr} = 0.2.

3.5 COMPARISON OF TWO-PHASE RADIAL FLOW MODEL WITH ZERO-DIMENSIONAL MODEL

Figure 3.4 compares the production enthalpies and reservoir temperatures simulated by TOUGH2 with those predicted by the zero-dimensional model for a vapor-dominated reservoir case with in-situ water saturation equal to 0.3. There appears to be a very good agreement between the simulation and the modeling results. TOUGH2 simulation results were then used to calculate the in-situ water saturation using Equation 3.5 as shown in the following calculation.

$$s_o = \frac{(1-\phi)}{\phi}\frac{\rho_r c_r (T_o - T_d)}{\rho_w (h_s - h_w)\big|_{T_o}} = \frac{(1-0.05)}{0.05}\frac{\left(2600\,{}^{kg}/_{m^3}\right)\left(0.485\,{}^{kJ}/_{kgC}\right)\left(280.0^{\circ}C - 266.5^{\circ}C\right)}{750.5\,{}^{kg}/_{m^3}\left(2780.4\,{}^{kJ}/_{kg} - 1236.8\,{}^{kJ}/_{kg}\right)} = 0.30$$

The zero-dimensional model gave the correct in-situ water saturation, which in this case is equal to the immobile water saturation. This result confirms that the zero-dimensional model can be used to infer both the in-place and immobile water saturation of vapor dominated geothermal reservoirs by knowing the initial and dry-out reservoir temperatures.

The TOUGH2 simulated reservoir temperatures agreed satisfactorily with the modeled temperatures. However, reservoir temperatures are not normally measured in the field. Instead, surface and downhole temperatures are routinely measured in the production wells. Figure 3.5 is a plot comparing TOUGH2 simulated downhole temperatures and modeled reservoir temperatures. The sudden initial drop in the downhole wellbore temperature as a response to production is clearly evident from the plot. After this early transient period, downhole temperatures decline at the same rate as the reservoir temperatures. TOUGH2 simulated downhole temperatures were then used to estimate the in-situ water saturation using Equation 3.5. The initial temperature, T_o, was taken to be the stable temperature after the early transient period.

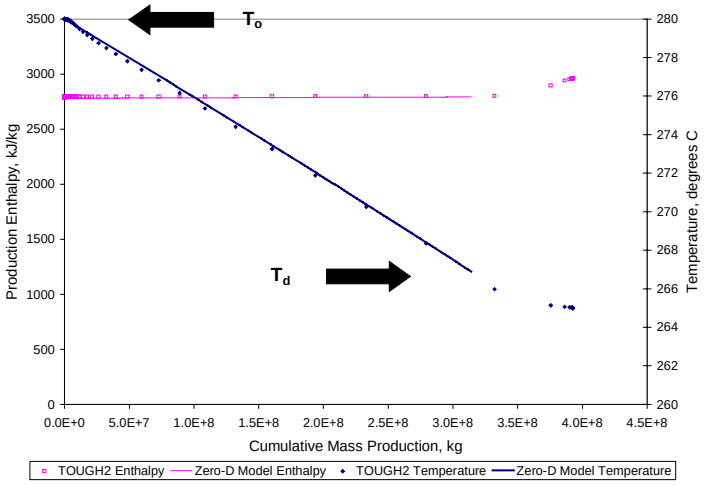

Figure 3.1: Production enthalpy and reservoir temperature profiles: s_{wi} = 0.3; s_{wr} = 0.3.

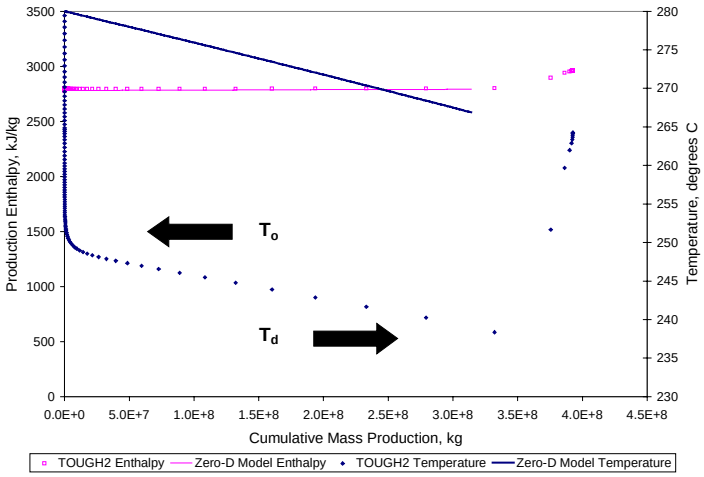

Figure 3.2: Production enthalpy and production temperature profiles: s_{wi} = 0.3; s_{wr} = 0.3.

The zero-dimensional model still gave a very close approximation of the correct in-situ water saturation as shown in the following calculation.

$$s_o = \frac{(1-\phi)}{\phi}\frac{\rho_r c_r (T_o - T_d)}{\rho_w (h_s - h_w)\big|_{T_o}} = \frac{(1-0.05)}{0.05}\frac{\left(2600\,{}^{kg}/_{m^3}\right)\left(0.485\,{}^{kJ}/_{kgC}\right)\left(251.5^{\circ}C - 238.0^{\circ}C\right)}{750.5\,{}^{kg}/_{m^3}\left(2780.4\,{}^{kJ}/_{kg} - 1236.8\,{}^{kJ}/_{kg}\right)} = 0.28$$

Therefore, either downhole wellbore or reservoir temperatures can be used to estimate the in-place water saturation using the zero-dimensional model. However, it is important that the stable initial, T_o, and dry-out, T_d, downhole temperatures be used in Equation 3.5.

$$s_o = \frac{(1-\phi)}{\phi}\frac{\rho_r c_r (T_o - T_d)}{\rho_w (h_s - h_w)\big|_{T_o}} \tag{3.5}$$

On the other hand, the response of liquid dominated geothermal reservoirs to exploitation can be described by a sequence of two-phase, dry saturated and superheated steam production. TOUGH2 and the zero-dimensional model predict similar trends in production enthalpy and temperature as illustrated in Figures 3.6 to 3.8. The enthalpy of

produced two-phase steam increases and reservoir temperature declines as the reservoir gets depleted of its mobile water. The production enthalpy then plateaus as the reservoir continues to dry out and produces dry saturated steam while the temperature continues to fall almost linearly. Finally, the enthalpy increases further as the reservoir completely dries out of immobile water and produces superheated steam.

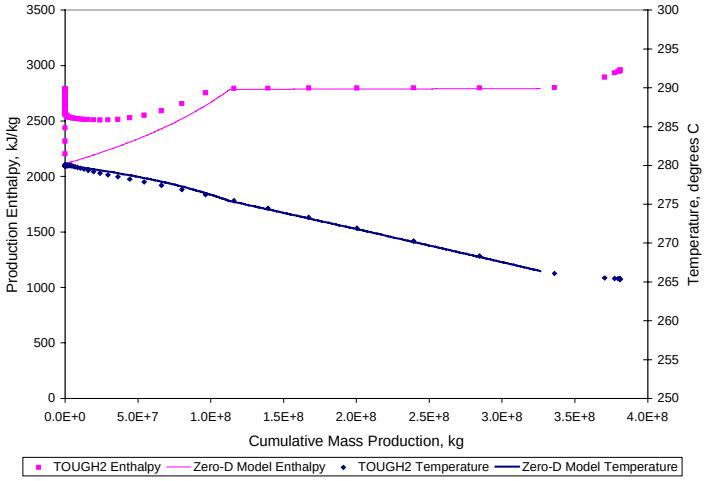

Figure 3.3: Production enthalpy and production temperature profiles: s_{wi} = 0.3; s_{wr} = 0.2.

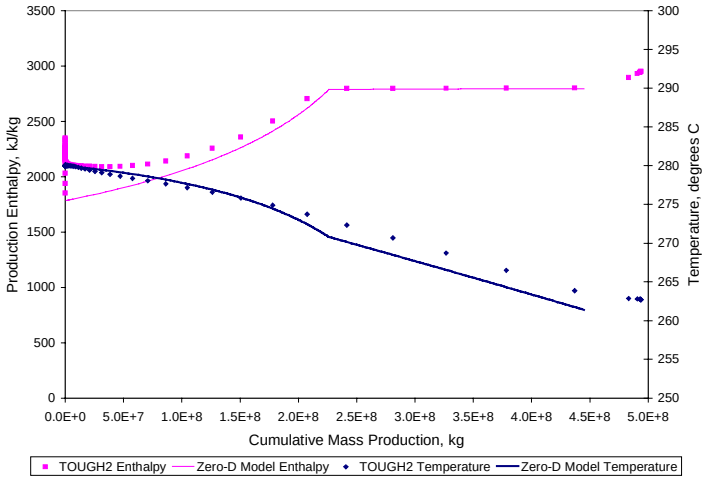

Figure 3.4: Production enthalpy and production temperature profiles: s_{wi} = 0.4; s_{wr} = 0.2.

However, the zero-dimensional model, which does not take into account both transient and spatial variations in temperature, pressure and saturation, fails to match the early transient two-phase production period predicted by TOUGH2. The zero-dimensional model predicts a continuous increase in two-phase steam enthalpy with cumulative mass production. On the other hand, TOUGH2 predicts a production period of apparently stable two-phase steam enthalpy immediately after the early transient period. Then the enthalpy increases with production until dry saturated steam is produced.

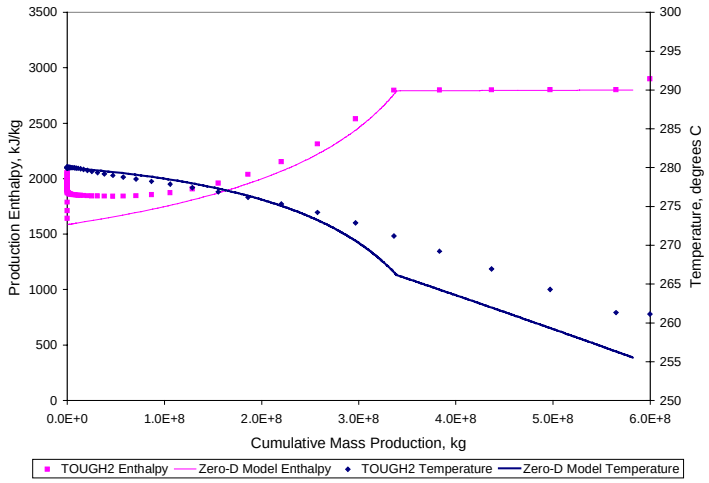

Figure 3.5: Production enthalpy and production temperature profiles: s_{wi} = 0.5; s_{wr} = 0.2.

Interesting observations can be made from the modeling results. Figures 3.9 and 3.10 are plots of production enthalpy and temperature for different values of in-situ water saturation and a fixed immobile water saturation. On the other hand, Figures 3.11and 3.12 are plots for different values of immobile water saturation and a fixed in-situ water saturation.

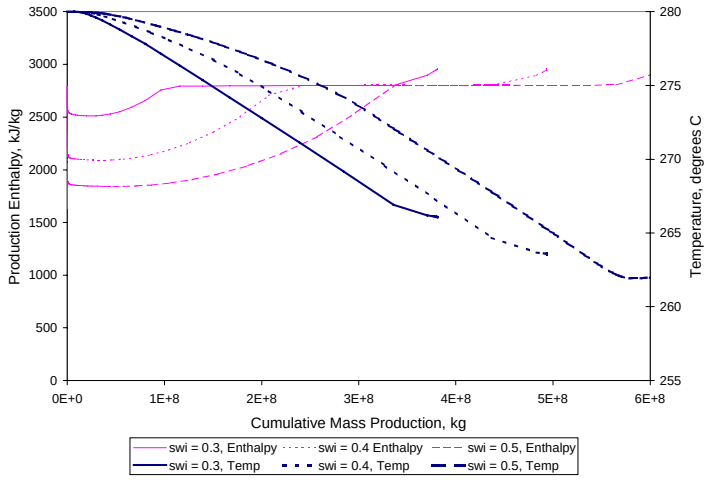

Figure 3.6: TOUGH2 simulated production enthalpy and reservoir temperature profiles: varying s_{wi}, constant s_{wr} = 0.2.

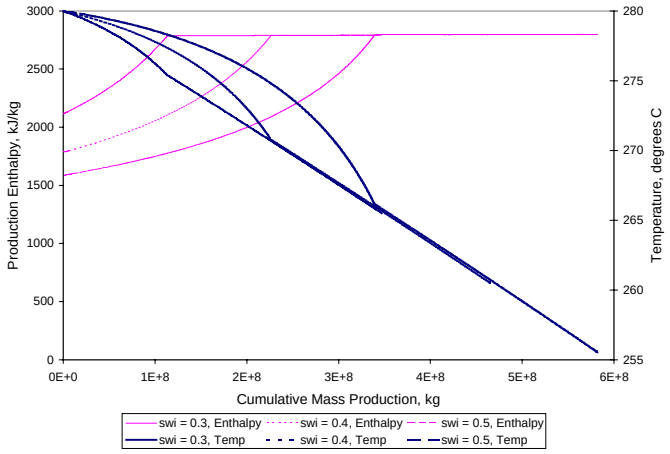

Figure 3.7: Zero-dimensional model production enthalpy and reservoir temperature profiles: varying s_{wi}, constant s_{wr} = 0.2.

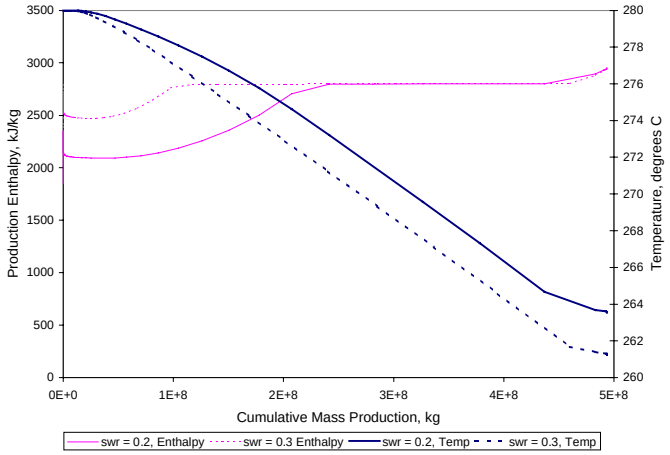

Figure 3.8: TOUGH2 simulated production enthalpy and reservoir temperature profiles: varying s_{wr}, constant s_{wi} = 0.4.

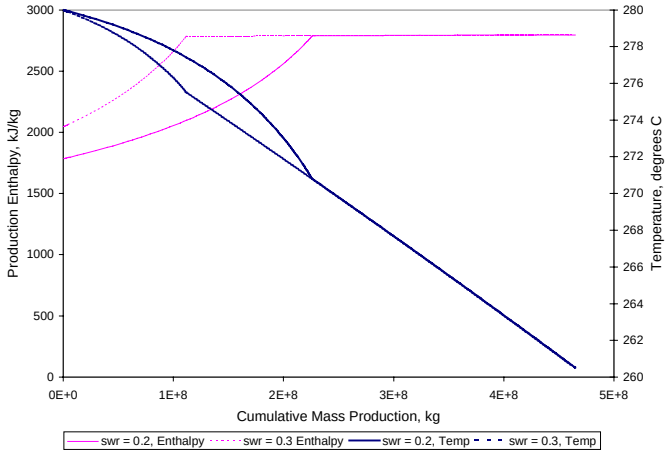

Figure 3.9: Zero-dimensional model production enthalpy and reservoir temperature profiles: varying s_{wr}, constant s_{wi} = 0.4.

Based on the modeling results, two-phase steam enthalpies are a function of the mobile water content of the reservoir, that is, the difference between the initial and immobile water saturation. Reservoirs with higher mobile water saturations produce two-phase steam with lower enthalpies. This is clearly evident from Figures 3.13 and 3.14, which show production enthalpies for cases of constant mobile water content but varying in-situ and immobile water saturation. Likewise, dry-out temperatures follow the same trend. Reservoirs with higher mobile water content dry-out at lower temperatures. Furthermore, dry saturated steam production commences at a later time in the life of a reservoir containing greater amount of mobile water.

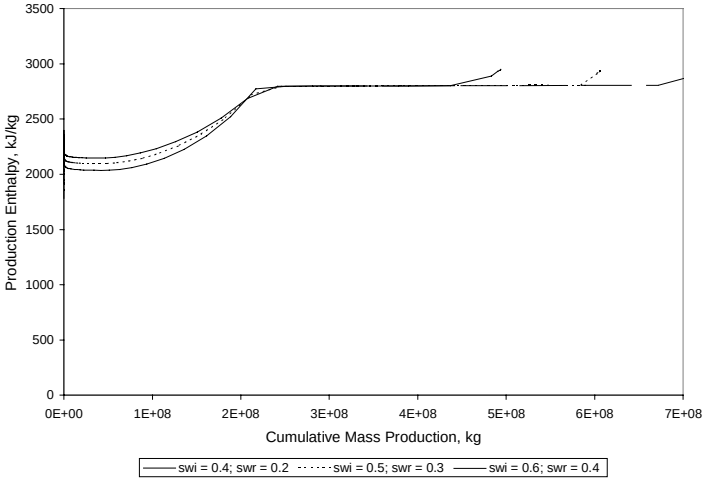

Figure 3.10: TOUGH2 simulated cumulative mass production and enthalpy profiles: mobile water content = 0.2.

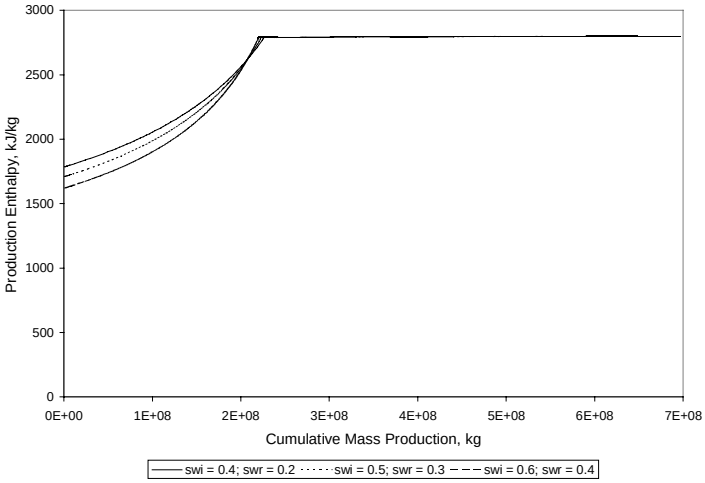

Figure 3.11: Zero-dimensional model cumulative mass production and enthalpy profiles: mobile water content = 0.2.

The mobile water content and the immobile water saturation of liquid-dominated geothermal reservoirs can then be inferred from the two-phase steam production enthalpy and the cumulative mass production using the zero-dimensional model. The discharge enthalpy of two-phase steam can be expressed as a weighted average of the individual steam and liquid water enthalpies given by Equation 3.12.

$$h' = \frac{\rho_w \frac{k_{rw}}{\mu_w} h_w + \rho_s \frac{k_{rs}}{\mu_s} h_s}{\rho_w \frac{k_{rw}}{\mu_w} + \rho_s \frac{k_{rs}}{\mu_s}} \tag{3.12}$$

Assuming that linear steam-liquid water relative permeability relations are valid, this equation can be rearranged to obtain an expression for the mobile water content in the reservoir,

$$\frac{s - s_{wr}}{1 - s_{wr} - s_{sr}} = \frac{\frac{\rho_s}{\mu_s}(h_s - h')}{\frac{\rho_w}{\mu_w}(h' - h_w) + \frac{\rho_s}{\mu_s}(h_s - h')} \tag{3.13}$$

Equation 3.13 can be used to calculate the ratio of the mobile water in the reservoir to the maximum possible mobile water. This ratio gives an indication of how much mobile water is present in the reservoir and how fast the reservoir is drying out. Similar expressions can be obtained by assuming different relative permeability relations.

The change in the reservoir saturation from an initial to a final state can be estimated using cumulative mass production data. The material balance equation describing two-phase steam production can be simplified to Equation 3.14 by assuming that the densities of steam and liquid water are approximately invariant with pressure and temperature. This equation gives the change in reservoir saturation as a function of the cumulative mass production, Δm, knowing the reservoir pore volume, ϕV.

$$\Delta s = s_1 - s_2 = \frac{\Delta m}{\phi V(\rho_w - \rho_s)} \tag{3.14}$$

The immobile water saturation can then be estimated based on the change in mobile water content from Equation 3.13 and the change in reservoir saturation from Equation 3.14. This technique is demonstrated below using fluid properties, and enthalpy and cumulative mass production values simulated by TOUGH2, as shown in Table 3.2. It is important to note that in using the model, the densities and viscosities of the two phases as well as the enthalpy of saturated steam are assumed to be invariant with pressure and temperature.

Table 3.2: Values obtained from TOUGH2 simulation.

T °C	h' kJ/kg	ρ_w kg/m^3	ρ_s kg/m^3	μ_w cp	μ_s cp	h_w kJ/kg	h_s kJ/kg
280	2144	750.5	33.2	0.55	0.11	1237	2780
274	2645	750.5	33.2	0.55	0.11	1070	2780

Calculate the mobile water content at the initial state using Equation 3.13.

$$\frac{s_1 - s_{wr}}{1 - s_{wr} - s_{sr}} = \frac{\frac{\rho_s}{\mu_s}(h_s - h')}{\frac{\rho_w}{\mu_w}(h' - h_w) + \frac{\rho_s}{\mu_s}(h_s - h')} = 0.1334$$

Calculate the mobile water content at the final state using Equation 3.13.

$$\frac{s_2 - s_{wr}}{1 - s_{wr} - s_{sr}} = 0.0185$$

Calculate the difference in mobile water between the initial and final states.

$$\frac{\Delta s}{1 - s_{wr} - s_{sr}} = \frac{s_1 - s_{wr}}{1 - s_{wr} - s_{sr}} - \frac{s_2 - s_{wr}}{1 - s_{wr} - s_{sr}} = \frac{s_1 - s_2}{1 - s_{wr} - s_{sr}} = 0.1149$$

Calculate the change in reservoir saturation using Equation 3.14.

$$\Delta s = s_1 - s_2 = \frac{\Delta m}{\phi V(\rho_w - \rho_s)} = \frac{8.13 \times 10^7 kg}{0.05(\pi \cdot 1000^2 \cdot 10 m^3)(750.5\,{}^{kg}/_{m^3} - 33.2\,{}^{kg}/_{m^3})} = 0.0722$$

Calculate the immobile water saturation based on the change in mobile water content and the change in reservoir saturation.

$$1 - s_{wr} - s_{sr} = \frac{\Delta s}{\frac{\Delta s}{1 - s_{wr} - s_{sr}}} = \frac{0.0722}{0.1149} = 0.63$$

$s_{sr} = 0.1$, *therefore*, $s_{wr} = 0.27 \approx 0.3$

3.6 CONCLUSIONS AND RECOMMENDATIONS

The in-situ and immobile water saturations can be inferred from field measurements of cumulative mass production, enthalpy and downhole temperature using simple zero-dimensional models developed based on material and energy conservation equations and Darcy's law. For vapor-dominated reservoirs, the in-situ and immobile water saturation can be estimated knowing rock and fluid properties, and the difference between the stable initial and the dry-out downhole temperatures and using Equation 3.5, repeated here.

$$s_o = \frac{(1-\phi)}{\phi} \frac{\rho_r c_r (T_o - T_d)}{\rho_w (h_s - h_w)\big|_{T_o}} \tag{3.5}$$

On the other hand, the in-situ and immobile water saturation of liquid-dominated reservoirs can be inferred from cumulative mass production, enthalpy, and downhole temperature data using Equations 3.13 and 3.14, repeated here.

$$\frac{s - s_{wr}}{1 - s_{wr} - s_{sr}} = \frac{\frac{\rho_s}{\mu_s}(h_s - h')}{\frac{\rho_w}{\mu_w}(h' - h_w) + \frac{\rho_s}{\mu_s}(h_s - h')} \tag{3.13}$$

$$\Delta s = s_1 - s_2 = \frac{\Delta m}{\phi V(\rho_w - \rho_s)} \tag{3.14}$$

The validity and usefulness of these zero-dimensional models were verified by comparing the modeling results with TOUGH2 two-phase radial flow simulation results. It is recommended that actual field production data be used to further verify the validity and usefulness of these models.

4. STEAM-WATER CAPILLARY PRESSURE

This research project is being conducted by Research Associate Kewen Li and Professor Roland Horne. The final objective of this project is to develop new techniques for estimating steam-water capillary pressure in geothermal systems. In this study the imbibition steam-water capillary pressures were calculated and compared with the drainage steam-water capillary pressures in the same Berea sandstone sample.

4.1 SUMMARY

The imbibition steam-water capillary pressures in a Berea sandstone sample were calculated using the technique developed by Li and Horne (2000). The results were compared with the drainage steam-water capillary pressures. The imbibition steam-water capillary pressure was less than the drainage steam-water capillary pressure. It was also confirmed experimentally that the lowering of vapor pressure in the porous medium studied was very small but the capillary pressure was significant for the experimental system used. This observation is consistent with thermodynamic analysis.

4.2 INTRODUCTION

In the January-March 2000 quarterly report, we described a method to calculate steam-water capillary pressure using a formula derived from Kelvin's equation with the measured pressures and temperatures of the water phase. The drainage steam-water capillary pressures in a Berea sandstone sample were also reported. In this quarterly report, we calculated the imbibition steam-water capillary pressures in the same sample using the method and compared with the drainage steam-water capillary pressures. The drainage curve has been fitted satisfactorily using the Brooks-Corey model and the imbibition curve has been described by a mathematical model suggested.

4.3 RESULTS

Using the Kelvin equation, steam-water capillary pressure can be calculated from the experimental data of liquid phase pressure, temperature, and related parameters. The procedure has been described in the quarterly report for January-March 2000.

The experimental details regarding the collection of the data used in this study have been described in Mahiya (1999).

The imbibition steam-water capillary pressures in the Berea sandstone sample have been calculated using the technique developed by Li and Horne (2000); the data are shown in Fig. 4.1. Also shown in Fig. 4.1 are the drainage steam-water capillary pressures from Li and Horne (2000). The imbibition steam-water capillary pressure at a water saturation of about 30% is around 3.5 psi which is much less than the drainage steam-water capillary pressure at the same water saturation. The imbibition capillary pressures are actually less than the drainage capillary pressures over the whole range of water saturation (see Fig. 4.1). This observation is consistent with that in gas-liquid systems. As an example, Leverett (1941) found that the imbibition air-water capillary pressure was less than the drainage capillary pressure in a sand pack.

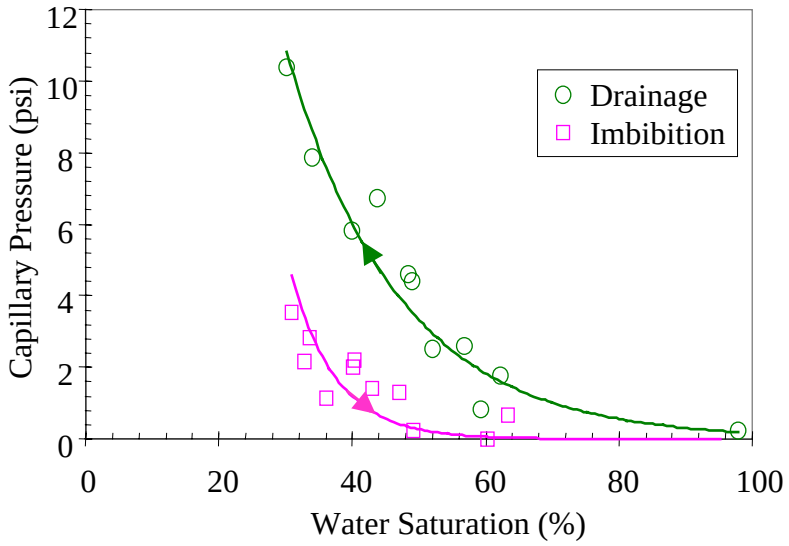

Figure 4.1: Steam-water capillary pressure curves in Berea sandstone.

The Brooks-Corey (1964) capillary pressure function is often used to model the drainage capillary pressure curve as given by:

$$P_c = p_e (S^*_{wd})^{-1/\lambda} \tag{4.1}$$

where P_c is the capillary pressure and p_e is the entry capillary pressure and λ is the pore size distribution index. S^*_{wd} is the normalized water saturation in the drainage case, defined as follows:

$$S^*_{wd} = \frac{S_w - S_{wr}}{1 - S_{wr}} \tag{4.2}$$

where S_w is the water saturation and S_{wr} is the residual water saturation by drainage.

We used the Brooks-Corey capillary pressure function to fit the experimental data. Fig. 4.2 shows a match to all the data of the drainage steam-water capillary pressure from this study using a value of 20% for S_{wr}. The values of the best-fit parameters are p_e = 0.425 psi and λ =0.543. The match for the drainage curve has an R-squared value of 0.819; the match to the experimental data is good.

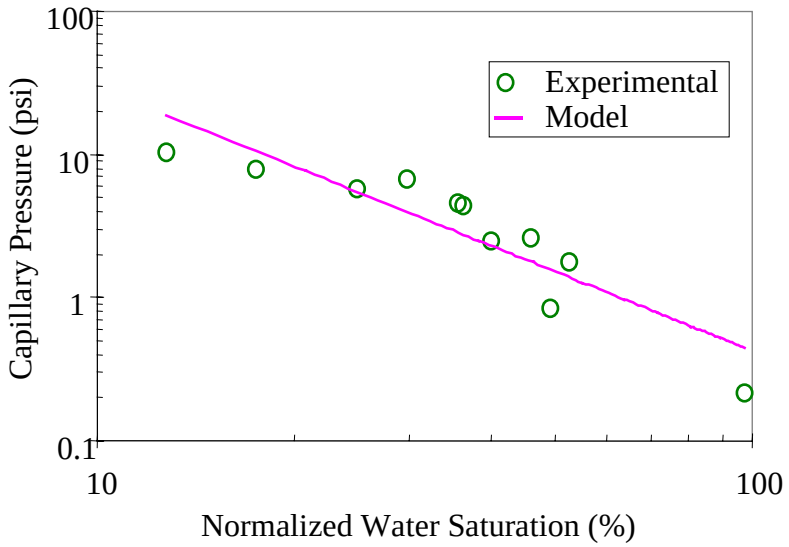

Figure 4.2: Normalized drainage steam-water capillary pressure curve in Berea.

Sinnokrot (1969) measured the oil-water capillary pressures of different rocks (limestones and sandstones) at different temperatures and found that the Brooks-Corey function could model the drainage oil-water capillary pressure curves but not the imbibition curves. Physically, it may not be appropriate to model imbibition capillary pressure curves using Eq. 4.1. For example, there should be no parameters such as entry pressure in an imbibition capillary pressure model. In order to model the imbibition curve of the steam-water capillary pressure, the normalized water saturation for an imbibition model is defined as follows:

$$S^*_{wimb} = \frac{S_w - S_{wi}}{1 - S_{wi} - S_{sr}} \tag{4.3}$$

where S_{wi} is the initial water saturation for imbibition, which is equal to the residual water saturation by drainage in this study. S_{sr} is the residual steam saturation by imbibition and S^*_{wimb} is the normalized water saturation for an imbibition capillary pressure model as given by:

$$P_c = p_m(1 - S^*_{wimb})^m \tag{4.4}$$

where p_m is the capillary pressure at S_{wi}; m is a fitting coefficient for the imbibition capillary pressure model.

Fig. 4.3 shows the match to the data of imbibition steam-water capillary pressures using Eq. 4.4, given that S_{sr} is equal to 13% (see Horne et al., 2000). The values of the best-fit parameters are p_m = 7.462 psi and m =4.572; the R-squared value is equal to 0.623.

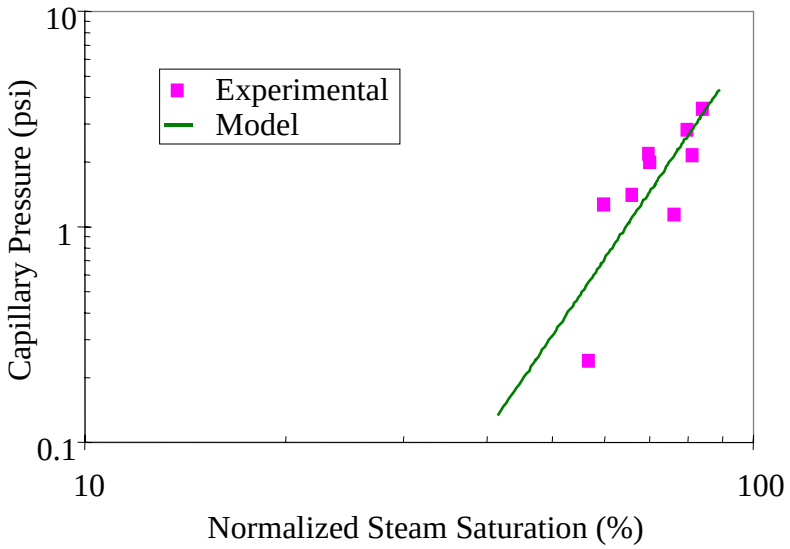

Figure 4.3: Normalized imbibition steam-water capillary pressure curve in Berea.

We can see from Figs. 4.2 and 4.3 that the drainage steam-water capillary pressure curve can be fitted satisfactorily using the Brooks-Corey model and the imbibition curve can be described by the suggested mathematical model (Eqs. 4.3 and 4.4). It would be useful for reservoir engineers to have such models to represent steam-water capillary pressure in numerical simulation and other engineering calculations.

The thermodynamics of single component vapor-liquid interfaces on flat surfaces may be different from that on curved surfaces. The vapor and liquid pressures in curved surface liquid-wet systems such as a steam-water-rock system may decrease, compared to those in a flat surface system. Which one, vapor pressure or liquid pressure, will decrease significantly? Fig. 4.4 plots the saturation pressures, which are equal to the vapor pressure on flat surfaces, and vapor pressures in Berea during both drainage and imbibition processes in steam-water flow. The vapor pressures are calculated using Eq. 4.5 (Li and Horne, 2000):

$$p_v - p_w = \frac{\rho_w RT}{M_w} \ln\left(\frac{p_0}{p_v}\right) \tag{4.5}$$

where p_0 is the vapor pressure when the vapor-liquid interface is flat; p_v is the vapor pressure in a capillary tube of radius r when the vapor-liquid interface is curved; p_w is the pressure of the liquid phase; R is the gas constant, T the absolute temperature, M_w the molecular weight of liquid, and ρ_w the density of liquid.

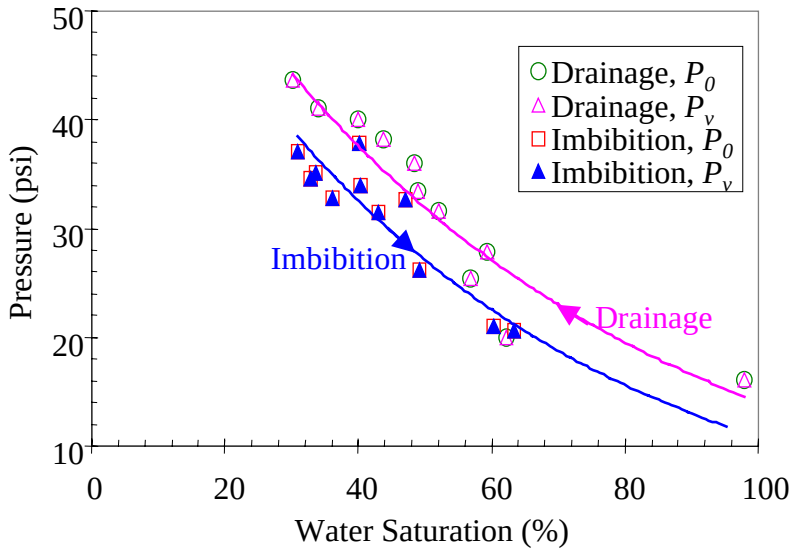

Figure 4.4: Saturation and vapor pressures during drainage and imbibition processes.

The lowering of vapor pressure in Berea is very small in either drainage or imbibition case (see Fig. 4.4). This phenomenon is consistent with the thermodynamic analysis by Udell (1982) who illustrated that the lowering of water vapor pressure was less than 1% for effective radii greater than 0.1 μm for all temperatures below the critical point and above the triple point. Sanchez and Schechter (1990) also mentioned that the lowering of vapor pressure was almost negligible. Since the steam-water capillary pressure in Berea is significant (see Fig. 4.1), the lowering of liquid pressure must also be significant. This observation demonstrates that the pressures of the liquid phase should be measured in order to obtain the steam-water or other kind of vapor-liquid capillary pressures using the Kelvin-based equations, as has been done in this study.

The observation that the lowering of vapor pressure in the porous medium is very small may not be always true. For example, the lowering of vapor pressure may be significant if the rock permeability is extremely low. In this case, the effective pore radii may be greater than 0.1 μm; therefore, the lowering of vapor pressure may be greater than 1% according to the conclusions of Udell (1982). For this type of rock, we may need to measure the pressures of the vapor phase.

Also shown in Fig. 4.4 is that the vapor pressure in the drainage case is greater than that in the imbibition case. The vapor pressure in either drainage or imbibition case decreases with the increase of water saturation, as expected.

4.4 DISCUSSION

In this study, we assumed that the pressures measured by the pressure transducers were the pressures of the water phase rather than the pressures of steam phase. The reasons are stated in the following discussion. Firstly, the rock used in this study was probably strongly water-wet (no wettability data for steam-water-rock systems are available yet);

therefore, there would be a trend for water in the tubing connected to the pressure transducers to imbibe into the core through the pressure ports. This would keep water around the pressure ports. The water phase was the continuous phase because the whole core system was initially saturated with water and the core was water-wet. Secondly, the measured pressures were either water or gas pressures. When we assumed that the measured pressures were the pressures of the gas phase, almost all the drainage steam-water capillary pressures calculated were negative, which is physically unreasonable. However, when we assumed that the measured pressures were the pressures of the water phase, the drainage steam-water capillary pressures computed were reasonable, as shown in Fig. 4.1. Collectively, these observations verified the appropriateness of the assumption that the pressures measured were the pressures of the water phase.

Another issue is the validity of using the Kelvin equation to calculate capillary pressure due to the differences between the pore shapes of the porous media and the circular shape that was assumed in the derivation of Eq. 4.5. Ward and Morrow (1987) measured air-water capillary pressure using a centrifuge method and a desorption method on the same core. They found that the capillary pressures measured by the centrifuge method agreed satisfactorily with results derived from the desorption isotherms using the Kelvin equation. Melrose (1991) and Melrose et al. (1994) compared different techniques to obtain capillary pressure data. They concluded that in the low saturation region, air-brine capillary pressure data obtained by the water-vapor-desorption technique using the Kelvin equation agreed with data obtained by the porous plate technique as well as the centrifuge technique. All these observations confirmed the appropriateness of using the Kelvin equation to calculate capillary pressure in certain cases.

Based upon the analysis of the differences between steam-water and nitrogen-water relative peremeabilities by Horne et al. (2000), we speculated that there could be significant differences between steam-water and air-water or nitrogen-water capillary pressures. It would be useful to identify how much the differences are. If there are no differences between steam-water and nitrogen-water capillary pressures or the differences are very small, we could measure nitrogen-water capillary pressure as a substitute for steam-water capillary pressure. The measurements of capillary pressure in air-water systems are very much easier to conduct. We have embarked on a project to measure the steam-water and air-water capillary pressures using the same rock sample in order to evaluate this issue.

4.5 CONCLUSIONS

Based on the present work, the following conclusions may be drawn:

1. The imbibition steam-water capillary pressure measured in the Berea sandstone sample is less than the drainage steam-water capillary pressure; this observation is consistent with that in gas-liquid systems.
2. The lowering of vapor pressure is very small but the steam-water capillary pressure is significant for the experimental system used.

3. The drainage steam-water capillary pressure curve can be described satisfactorily using the Brooks-Corey model and the imbibition curve can be described by a mathematical model suggested here.

4.6 FUTURE WORK

The next step is to measure the steam-water and air-water capillary pressures using the same rock sample in order to identify the differences between them.

5. SPONTANEOUS WATER IMBIBITION

This research project is being conducted by Research Associate Kewen Li and Professor Roland Horne. The objective of this project is to develop a method to evaluate the feasibility of water injection into geothermal reservoirs. As a preliminary step, the experiments have been conducted in air-water-rock systems using rocks from The Geysers as well as Berea sandstone.

5.1 SUMMARY

One of the most important concerns in the geothermal industry in recent years is reservoir decline. Injection of condensate and waste water in geothermal reservoirs is an important and practical solution. Is there any method to study the feasibility of water injection into geothermal reservoirs in advance of implementing liquid injection? How can we identify the difference of water injectability between different reservoirs? Spontaneous water imbibition tests in rocks from The Geysers and in Berea sandstone have been designed to answer these questions. The maximum water saturation and the maximum imbibition rate by spontaneous water imbibition were used to evaluate the feasibility and the ability of water injection into geothermal reservoirs. Reservoirs with high imbibition rates and high maximum water saturation are good candidates for water injection. If there is no imbibition of water into the rocks at all, then the reservoir is not suitable for water injection. The relationships between imbibition rate and time for The Geysers rocks have been measured under countercurrent and cocurrent imbibition conditions, respectively. The measured maximum water saturation by the spontaneous water imbibition in The Geysers rock was about 87.9%, which was much greater than that in Berea although the imbibition rate was lower. Experimental results showed that The Geysers geothermal reservoir is appropriate for water injection, which has been confirmed by the practice of water injection in the field itself.

5.2 INTRODUCTION

Injection of condensate or waste water in geothermal reservoirs is usually deployed in geothermal reservoirs to maintain reservoir pressure and protect against environmental impact. Spontaneous water imbibition is a dominant process during injection into these reservoirs. It would be useful for geothermal reservoir engineers to have a method or some set of criteria to appraise the feasibility of water injection into geothermal reservoirs prior to the implementation. Unfortunately, few experimental approaches are available in the literature. Therefore, spontaneous water imbibition tests in rocks from The Geysers have been designed and a model has been modified to assess water injection projects. The idea was the following: if we could model the spontaneous water imbibition process mathematically, then we could derive a formula to represent the relationship between the water imbibition rate (q_w) and the imbibition time (t). It might then be possible to upscale the experimental results to field scale by using the mathematical model once the average fracture spacing was known. Therefore, we would be able to forecast the water injection performance in geothermal reservoirs.

The critical issue is how to model the spontaneous water imbibition process in geothermal rocks. There are a lot of papers in the literature regarding spontaneous water

imbibition into oil-saturated sandstone samples but few in gas-saturated geothermal rocks. The study of spontaneous water imbibition is essential to predict the production performance in these reservoirs where the amount and rate of mass transfer between the matrix and the fracture influence the recovery and the production rate. Experimental data may be used to evaluate the feasibility of water injection into geothermal reservoirs. Since spontaneous imbibition is a capillary-pressure dominated process, the imbibition rate depends significantly on the properties of the porous media, the fluids, and the interactions between the two. These include permeability and relative permeability of the porous media, pore structure, matrix sizes, shapes and boundary conditions, fluid viscosities, initial water saturation, the wettability of the rock-fluid systems, and the interfacial tension between the imbibed phase and the resident phase. Aronofsky et al. (1958) suggested an empirical form of the function of time relative to production from the matrix volume:

$$\eta = 1 - e^{-\lambda t} \tag{5.1}$$

where η is the recovery in terms of recoverable resident fluid by spontaneous water imbibition, λ is a constant giving the rate of convergence, and t is the imbibition time. Schechter and Guo (1998) used a similar equation to fit the experimental data of spontaneous water imbibition in oil-saturated rocks by substituting t with the dimensionless time t_D, which is defined as follows:

$$t_D = t\sqrt{\frac{k}{\phi}}\frac{\sigma\cos(\theta)}{\mu_m L_c^2} \tag{5.2}$$

where k is the rock permeability, σ is the interfacial tension between oil and water, ϕ is the porosity, θ is the contact angle, μ_m is the geometric mean of water and oil viscosities and L_c is the characteristic length and defined as follows (Ma et al., 1995):

$$L_c = \sqrt{\frac{V}{\sum_{i=1}^{n}\frac{A_i}{X_{Ai}}}} \tag{5.3}$$

here V is the bulk volume of the matrix, A_i is the area open to imbibition at the ith direction, and X_{Ai} is the distance traveled by the imbibition front from the open surface to the no-flow boundary. Another method used to model the process of spontaneous water imbibition into gas-saturated rocks is the Handy equation (Handy, 1960):

$$N_{wt}^2 = A^2\frac{P_c k_w \phi S_{wf}}{\mu_w}t \tag{5.4}$$

where A and N_{wt} are the cross-section area of the core and the volume of water imbibed into the core, respectively; μ_w is the viscosity of water; S_{wf} is the water saturation behind the imbibition front. k_w is the effective permeability of water phase at a water saturation of S_{wf}. P_c is the capillary pressure at S_{wf}. As discussed by Schembre et al. (1998), $P_c k_w S_{wf}$ might be referred to as the imbibition potential. According to the Handy equation, the amount of water imbibed into porous media is infinite when imbibition time approaches infinity, which is physically impossible.

Li and Horne (2000) developed a method to calculate the capillary pressure and relative permeability at S_{wf} from spontaneous water imbibition data. This method was verified experimentally in sandstone with high permeability but not yet in very low permeability rocks.

In Eq. 5.1, η is the recovery in terms of recoverable resident fluid by spontaneous water imbibition. It is necessary to obtain the value of the residual gas saturation (S_{gr}) or the maximum water saturation (S_{wmax}) in order to calculate η. However, the residual gas saturation may not be available in certain cases. Therefore, we modified Eq. 5.1 as follows:

$$\eta^* = \frac{1 - S_{wi} - S_{gr}}{1 - S_{wi}} (1 - e^{-\lambda t_D}) \tag{5.5}$$

where η^* is the gas recovery in terms of gas originally in place (GOIP). S_{wi} and S_{gr} are the initial water saturation and the residual gas saturation in rocks. λ and S_{gr} can be obtained simultaneously using a history match technique with the experimental data from spontaneous water imbibition. In this study, S_{wi} was equal to zero.

As a preliminary study, spontaneous water imbibition tests in air-saturated rocks from The Geysers have been conducted under both countercurrent and cocurrent imbibition conditions. The amount of water imbibed as a function of time has been measured. The experimental data of water imbibition rate have been up-scaled using the modified model (Eq. 5.5), which may be applied to design water injection projects for geothermal reservoirs. The experimental results of spontaneous water imbibition in the rocks from The Geysers geothermal field are compared with those in Berea sandstone with much higher permeability.

5.3 EXPERIMENTS

In this study, distilled water was used as the liquid phase and air was used as the gas phase. The surface tension of water/air at 20^{o}C is 72.75 dynes/cm. The Geysers rock sample from a depth of 1410.1m was obtained from the Energy and Geoscience Institute; its porosity was about 4.5%. The matrix permeability of the rock sample has not been determined yet. The permeability of a nearby sample measured by nitrogen injection was about 0.56 md (after calibration of the gas slip effect), which is probably attributable mainly to the fracture permeability. The length and diameter of this rock sample were

3.52 cm and 8.25 cm. The permeability and porosity of the Berea sandstone sample were around 1200 md and 24.5%; its length and diameter were 43.5 cm and 5.06 cm.

The apparatus to conduct spontaneous water imbibition tests in air-saturated porous media is the same as that described in Li and Horne (2000). A schematic of the apparatus is shown in Fig. 5.1. The Geysers rock sample was hung under a Mettler balance (Model PE 1600) which had an accuracy of 0.01g and a range from 0 to 1600g. The water imbibed into the core sample was recorded in time by the balance using an under-weighing method and the real-time data were measured continuously by a computer through an RS-232 interface. The purpose of using the under-weighing method is to reduce the experimental error caused by water evaporation. Since the Berea sandstone sample was longer and heavier than The Geysers rock, its weight was beyond the range of the Mettler balance so another balance (Sartorius, Model BP6100) with a larger capacity was used instead. This balance had an accuracy of 0.1g and a range from 0 to 6100 g.

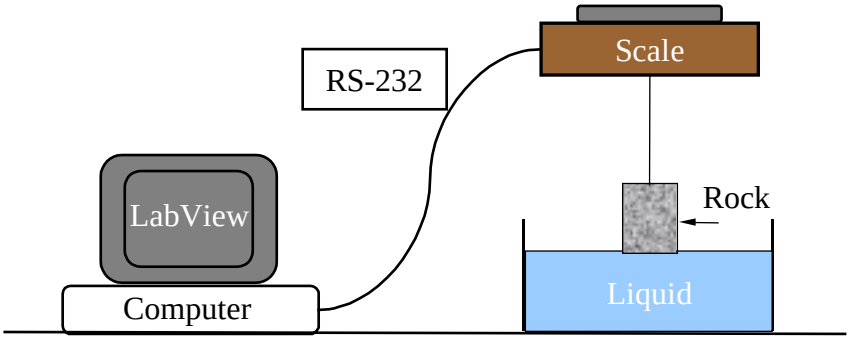

Figure 5.1: Schematic of apparatus for spontaneous water imbibition test.

Rock samples were dried by heating at a temperature of around 105^{o}C until their weight did not vary during eight hours. The core sample was wrapped from the side using a heat-shrink tubing after it was cooled down and then assembled in the apparatus as shown in Figure 5.1. Water started to imbibe into the core when its base touched the water surface in the cocurrent water imbibition tests. The weight change of the core sample was then recorded with time. Figure 5.1 represents the case for cocurrent water imbibition tests at room temperature. For countercurrent water imbibition tests, the whole rock was immersed in the water. The procedure of countercurrent water imbibition was similar to that of the cocurrent imbibition except that the water level was over the top surface of the rock.

5.4 RESULTS

Spontaneous water imbibition tests in the air-saturated rock from The Geysers were conducted at room temperature under both cocurrent and countercurrent conditions. The experimental results and discussion are presented in this section.

Fig. 5.2 plots the amount of water imbibition into the air-saturated Geysers rock as a function of time under both cocurrent and countercurrent conditions. The cumulative amount of water imbibed into the rock represented as the fraction of pore volume is equal to the water saturation in the rock or the gas recovery because the initial water saturation is equal to zero in this study. Fig. 5.2 shows that the values of the ultimate gas recovery were almost the same in both cocurrent and countercurrent imbibition cases. The value of the maximum water saturation in the rock from The Geysers by either cocurrent or countercurrent water imbibition is about 87.9% (see Fig. 5.2). The maximum water saturation in a rock may be used as a parameter to evaluate the capacity of water injection into geothermal reservoirs. Evidently, the greater the maximum water saturation, the larger the capacity of water injection. Li and Horne (2000) found that maximum water saturation in sandstone was not affected by the initial water saturation and was about 66.5%. We can see that maximum water saturation changes significantly with rock properties according to the comparison of the value in Berea by Li and Horne (2000) to that in The Geysers rock here. This provides support for the use of maximum water saturation as a parameter to evaluate the capacity of water injection into geothermal reservoirs.

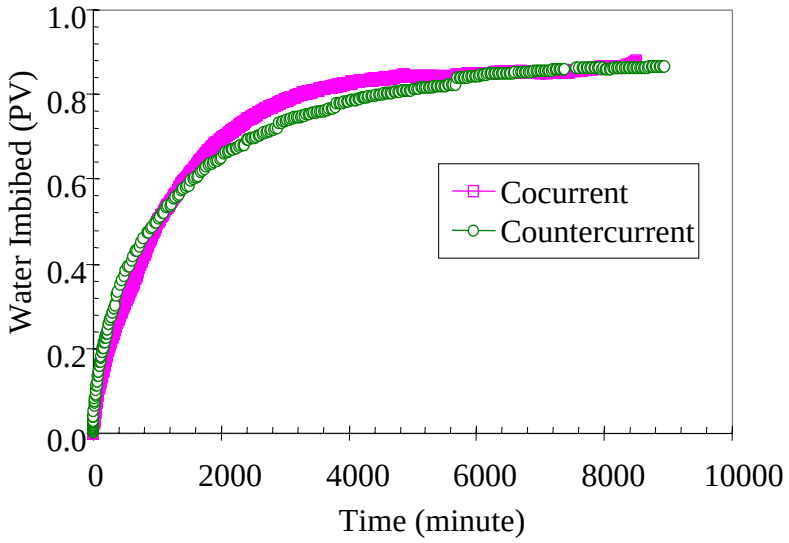

Figure 5.2: Water imbibed vs. time under countercurrent and cocurrent conditions.

The water imbibition rate vs. time is shown in Fig. 5.3. At early time, it was difficult to record water imbibition data accurately (Li and Horne, 2000), so the water imbibition rate data at early time is scattered. However, we can see on Fig. 5.3 that the water imbibition rate under countercurrent conditions was higher than that under cocurrent condition at early time and lower at later time. Bourblaux and Kalaydjian (1990) reported that the oil recovery by countercurrent water imbibition was slower than that by cocurrent water imbibition in a sandstone core with a permeability of around 120 md and a porosity of 23%. Zhang et al. (1996) observed a similar phenomenon in oil-water-Berea systems but they also found that the difference between countercurrent and cocurrent water imbibition was small in some cases. There may be differences in water imbibition between gas-

water and oil-water systems. Unfortunately, few experimental data are available in the literature regarding the comparison of water imbibition behavior in the two different systems. On the other hand, the rock sample from The Geysers geothermal field had very low porosity and permeability. This might also influence the water imbibition behavior under cocurrent and countercurrent conditions. Further investigation is necessary in this area.

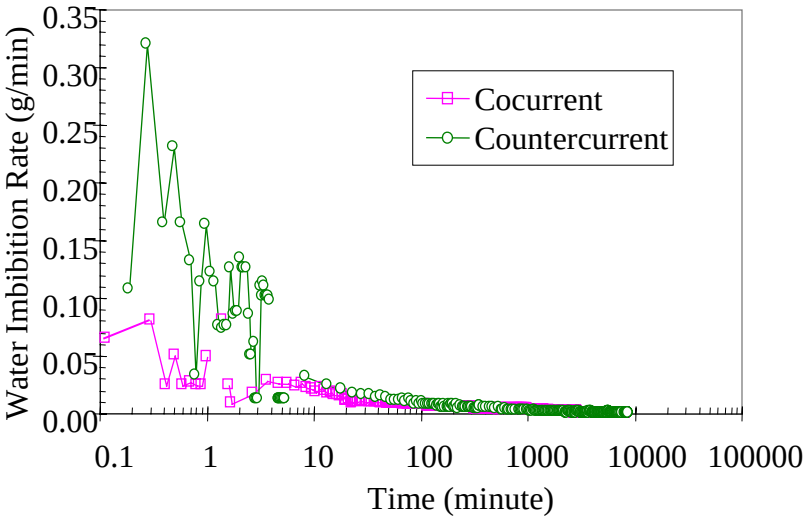

Figure 5.3: Water imbibition rates under countercurrent and cocurrent conditions.

Scaling up the experimental data of spontaneous water imbibition in gas-water systems is still a challenge. One possible approach is to deploy the scaling group as represented in Eq. 5.2, which is for oil-water systems. We substituted the average viscosity with the water viscosity here. Fig. 5.4 shows the relationship between the water imbibed and the dimensionless time represented by Eq. 5.2. Also shown in Fig. 5.4 is the history match to the experimental data using Eq. 5.5.

The value of S_{gr} obtained by the history match to cocurrent data is about 14.6%; λ is about 0.002177. From the countercurrent data, S_{gr} is about 17.1%; λ is about 0.000595. The match to the cocurrent data is a little better than to the countercurrent data. However, there are obvious differences between the cocurrent and countercurrent water imbibition by using the scaling group represented by Eq. 5.2. Zhang et al. (1996) verified experimentally that cocurrent and countercurrent water imbibition data could be scaled up in oil-water systems. Fig. 5.4 shows that the scaling group represented by Eq. 5.2 may not be suitable for gas-water systems in a rock such as from The Geysers.

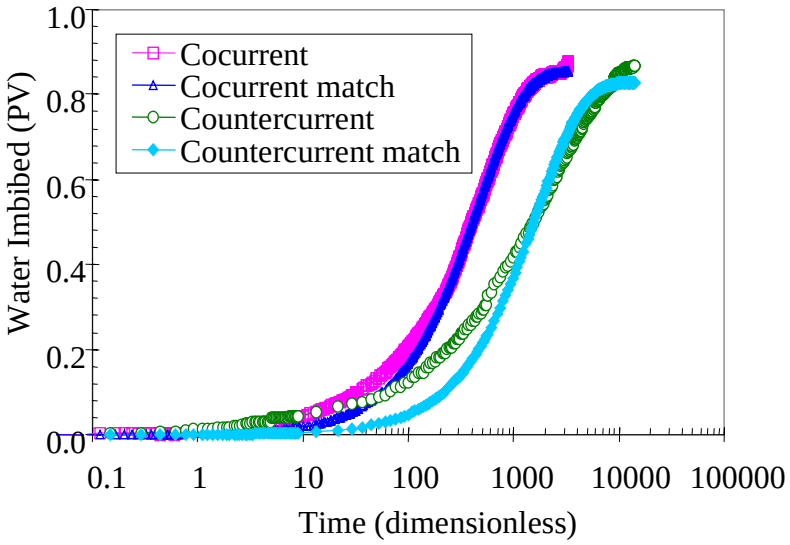

Figure 5.4: Water imbibition rate vs. dimensionless time.

Although Fig. 5.4 shows differences in the imbibition behavior between the cocurrent and countercurrent water imbibition, we speculate that the actual water imbibition at reservoir scale may be intermediate between the two. Therefore, we constituted an empirical model for the spontaneous water imbibition into the rock from The Geysers using the average values of S_{gr} and λ as follows:

$$\eta^* = \frac{1 - S_{wi} - 0.1585}{1 - S_{wi}} (1 - e^{-0.00139 t_D}) \tag{5.6}$$

The water imbibition rate at reservoir scale is obtained from Eq. 5.6 as follows:

$$q_w = 0.00139 V_p \frac{1 - S_{wi} - 0.1585}{1 - S_{wi}} \sqrt{\frac{k}{\phi}} \frac{\sigma \cos\theta}{\mu_w L_c^2} e^{-0.00139 t_D} \tag{5.7}$$

where V_p is the pore volume of the reservoir and q_w is the water imbibition rate. The characteristic length for a matrix block in the reservoir is half the fracture spacing for countercurrent water imbibition. According to Eq. 5.7, we can calculate the water imbibition rate once porosity, permeability, surface tension and fracture spacing are known. The contact angle may be assumed zero in gas-water systems. The maximum water imbibition rate (q_{wmax}) may be an important parameter to evaluate the feasibility of water injection into geothermal reservoirs. q_{wmax} can be calculated using Eq. 5.7 (t_D=0). Note that the coefficient will be different if different units are used for the parameters in Eq. 5.7. For geothermal reservoirs with different rock properties, obviously, a reservoir that has large q_{wmax} is a good candidate for water injection. The practical water injection rate in geothermal reservoirs is likely to be less than the calculated q_{wmax}. Otherwise most of the injected water would be produced very quickly from the production wells through

the highly distributed fractures before the water imbibes into the matrix blocks, which is not what we would like.

Fig. 5.5 shows the comparison of the relationship between the water imbibed in the rock from The Geysers and that in Berea sandstone under cocurrent conditions. S_{wmax} by spontaneous water imbibition in Berea is much less than that in the rock from The Geysers. There is significant difference of water imbibition behavior between Berea and the rock from The Geysers. Fig. 5.5 also demonstrates the difficulty in scaling up spontaneous water imbibition data in gas-water systems for different rocks by using the scaling group of dimensionless time represented in Eq. 5.2.

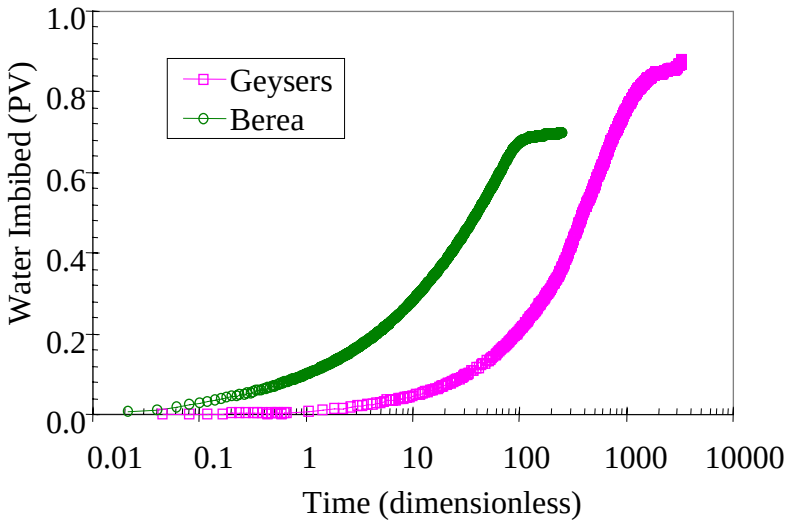

Figure 5.5: Water imbibed vs. dimensionless time in Berea and The Geysers.

The relationships between the water imbibition rate and the dimensionless time for both Berea and The Geysers rocks are shown in Fig. 5.6. As we observed experimentally, the water imbibition rate in Berea is much higher than that in The Geysers rock. Note that the unit of the water imbibition rate in Fig. 5.6 is pore volume per dimensionless time instead of per minute.

Is The Geysers field suitable for water injection according to the water imbibition data in comparison to that in Berea? The answer may be “yes”. The measured maximum water saturation in The Geysers was about 87.9%, which was much greater than that in Berea although the imbibition rate was lower. The large value of the measured maximum water saturation implies that the rock in The Geysers may be strongly water-wet (Li and Firoozabadi, 2000). Injected water can imbibe into the matrix rocks instead of bypassing directly from the injectors to the producers through fractures. The successful practice of water injection into The Geysers to maintain reservoir pressure and protect the environment also demonstrates that water injection is appropriate for The Geysers geothermal field (Goyal, 1999).

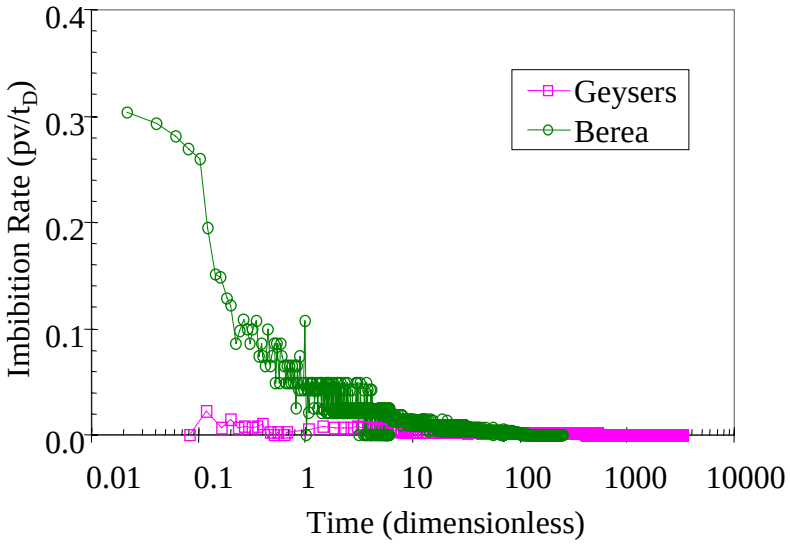

Figure 5.6. Water imbibition rate vs. dimensionless time in Berea and The Geysers.

There may be a discrepancy between the use of maximum water saturation and imbibition rate to evaluate the feasibility of water injection. The measured maximum water saturation in The Geysers was much greater than that in Berea, which was positive for water imbibition in The Geysers; but the water imbibition rate was much lower, which was not positive for water imbibition in The Geysers.

There may be some differences between water imbibition in air-water and steam-water systems. Therefore, we have embarked on a project to investigate spontaneous water imbibition in steam-saturated rocks at high temperatures using rocks from different geothermal fields. We are investigating the effect of rock properties such as porosity, permeability, and wettability on the maximum water saturation and water imbibition rate.

5.5 CONCLUSIONS

Based on the present work, the following conclusions may be drawn:

1. An experimental technique has been developed to evaluate the feasibility of water injection into geothermal reservoirs.
2. The maximum water saturation or the residual gas saturation and the maximum water injection rate have been suggested as the parameters for the evaluation. The geothermal reservoirs with large values of maximum water saturation and maximum water imbibition rate are good candidates for water injection.
3. The residual gas saturation by spontaneous water imbibition in the rock from The Geysers was about 12.1%, which is a small value.
4. Little difference between cocurrent and countercurrent spontaneous water imbibition was observed; the ultimate recovery was almost the same in the rock from The Geysers.
5. The maximum water saturation in The Geysers was much greater than that in Berea although the imbibition rate was lower.

6. The experimental data demonstrate that The Geysers geothermal field is appropriate for water injection, which has been confirmed by the successful practice of water injection in the field.

5.6 FUTURE WORK

We are developing the apparatus for conducting spontaneous water imbibition in steam-water systems instead of air-water systems.

6. EXPERIMENTAL INVESTIGATION OF STEAM AND WATER RELATIVE PERMEABILITY IN SMOOTH-WALLED FRACTURES

This project is being conducted by Research Assistant Gracel P. Diomampo, Research Associate Kewen Li and Prof. Roland Horne. The goal is to gain better understanding of steam-water flow through fractured media and determine the behavior of relative permeability in fractures.

6.1 BACKGROUND

Geothermal reservoirs are complex systems of porous and fractured rocks. Complete understanding of geothermal fluid flow requires knowledge of flow in both types of rocks. Many studies have been done to investigate steam and water flow through porous rocks. This is not the case for multiphase flow in fractures. Only a few published data are available most of which have been done for air-water system or for water-oil systems. Earliest is Romm's (1966) experiment with kerosene and water through an artificial parallel-plate fracture lined with strips of polyethylene or waxed paper. Romm found a linear relationship between permeability and saturation, $S_w = k_{rw}$, $S_{nw} = k_{rnw}$ such that $k_{rw}+k_{rnw} = 1$. Pan et al. (1996) performed a similar experiment with an oil-water system but arrived at conflicting results. Significant phase interference was observed such that $k_{rw} + k_{rnw} < 1$. Both studies, however, conclude that residual saturations are zero such that a discontinuous phase can flow as discrete units along with the other phase.

In an attempt to develop a relationship between fracture relative permeability and void space geometry, Pruess and Tsang (1990) conducted numerical simulation for flow through rough-walled fractures. The study showed that the sum of the relative permeabilities is less than 1, residual saturation of the nonwetting phase is large and phase interference is greatly dependent on the presence or absence of spatial correlation of aperture in the direction of flow. Persoff et al. (1991) did experiments on gas and water flow through rough-walled fractures using transparent casts of natural fractured rocks. The experiment showed strong phase interference similar to the flow in porous media. Data of Persoff (1991) and Persoff and Pruess (1995) for flow through rough-walled fractures were compared in Horne et al. (2000), as shown in Figure 6.1.

Presently, the mechanism of flow and the characteristic behavior of relative permeability in fractures are still undetermined. Issues such as whether a discontinuous phase can travel as discrete units carried along by another phase or will be trapped as residual saturation as in porous medium are unresolved. The question of phase interference i.e. is the relative permeability curve against saturation an X-curve, Corey or some other function is still unanswered. The main objective of this study is to contribute to the resolution of these issues. Experiments on flow through smooth-walled fractures will be done first for air-water flow with the aim of establishing a reliable methodology for flow characterization and permeability calculation. Then these experiments will be done with a steam-water system; and with rough-walled fractures.

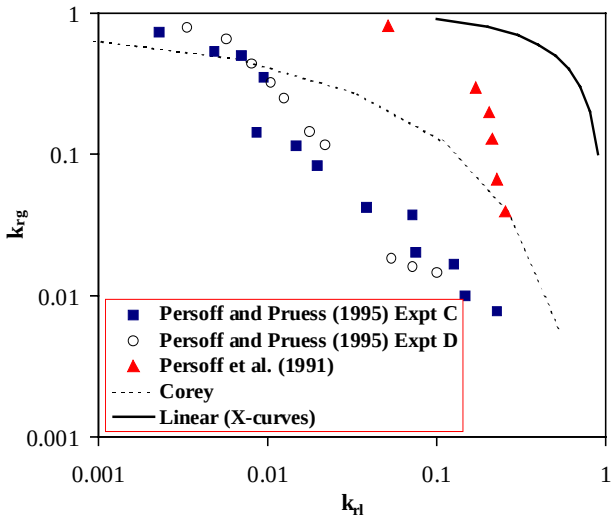

Figure 6.1: Some measurements of air-water relative permeabilities in rough-walled fractures (graph from Horne et al., 2000).

6.2 EXPERIMENTAL APPARATUS AND MEASUREMENT TECHNIQUES

The apparatus consisted of a 183 cm. by 31 cm of horizontal glass plate on top of an aluminum plate. The aperture was set by 0.2-mm thick shims inserted between the glass and aluminum plates. The shims were placed along the boundaries and in three columns along the flow area. It should be noted that the shims placed as columns along the plate did not isolate the plate into separate flow sections. This was deduced upon observing cross flow along the shims.

The sides of the plates were sealed together with a silicone adhesive. It was observed that even with the adhesive, the inlet head had to be kept below 15 cm to avoid leakage. This presented a maximum limit in the flow rates approximately 2 cc/sec for water and 9 cc/sec for nitrogen.

Horizontal slits in the ends of the metal plate served as entry and exit points for the fluids. There are two available canals for input of gas and liquid. The approaches of injecting nitrogen and water as separate streams or as mixed fluid in a single stream were tried. It was found that mixing the gas and water prior to input caused no significant improvement in fluid distribution. Thus, the gas and water streams were injected separately for simplicity, ease of flow rate control and inlet pressure reading.

Gas flow was controlled through a flow regulator. A meter pump controlled the rate of liquid injection. Dye was dissolved in the injection reservoir for better phase identification. Figure 6.2 is a schematic diagram of this configuration.

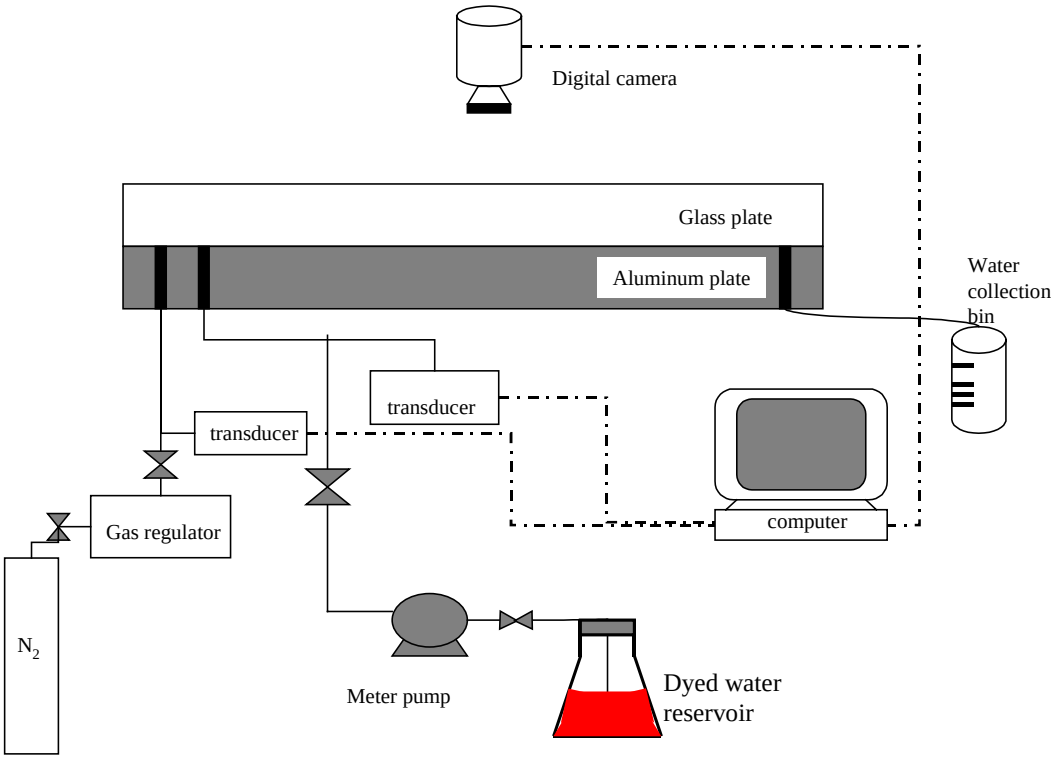

Figure 6.2: Experimental set-up for air and water flow through smooth walled fractures.

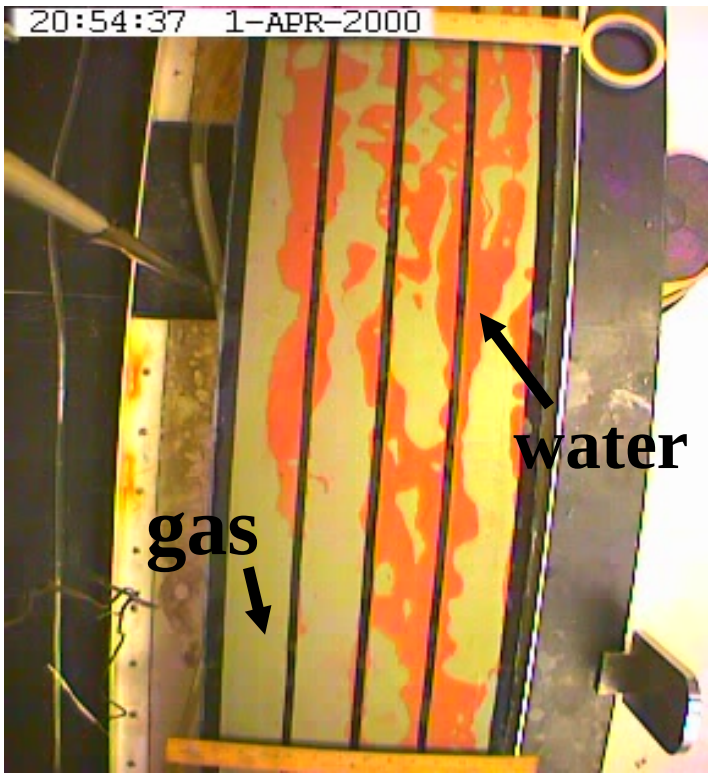

Figure 6.3: Sample camera image for two-phase run.

Low capacity transducers measured the gas and liquid inlet pressure separately. These transducers are connected to a Labview program designed to record data at specified time intervals. Water rate is read from the pump meter and gas rate from the regulator. Saturation was computed by measuring the area that each phase occupied. This was done by taking digital photographs of a constant area of the plate at a particular gas and water rate. The area was around 3 ft. long. The region was chosen far enough from the ends of the plates to avoid end effects. Figure 6.3 shows a sample photograph of a two-phase run. The photographs were processed in a Matlab program which uses quadratic discriminant analysis to group the pixels of the photograph into three groups: the water phase, the gas phase and the shim. The grouping was based on color differences. Saturation was calculated as total pixels of liquid group over the sum of the gas and liquid group. Figure 6.4 shows a comparison of the gray scaled image produce by the program and the original photograph from the digital camera. The accuracy of the program in calculating the saturation can be related to the similarity in details of the gray scale image to the true image. From the figure, it can be said that the program has reasonable accuracy.

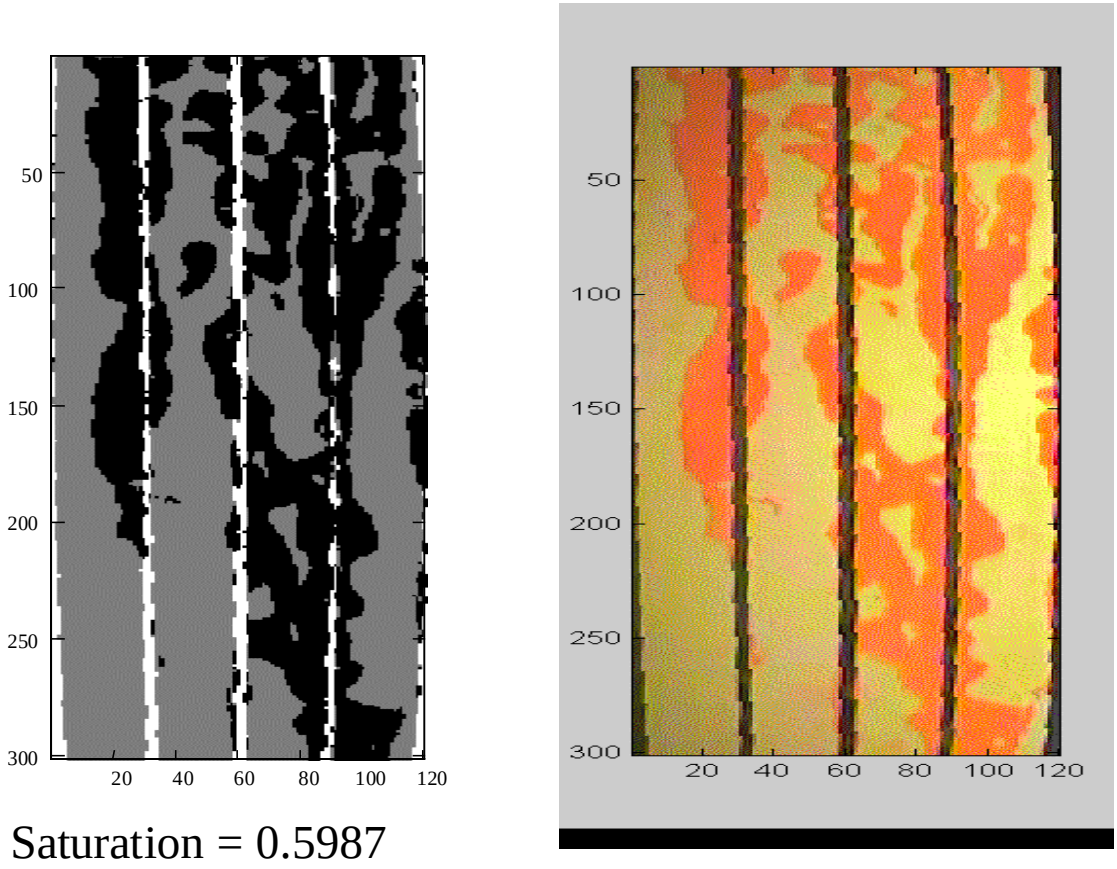

Figure 6.4: Comparison of gray image produced by Matlab program (left) to actual photo taken by digital camera (right).

Pan et al. (1996) also used this technique for measurement of saturation. This study noted that the sources of error in this technique were the quality of the photographs and the water film adsorbed on the surfaces of the plates with the latter being of minimal

effect. Good quality photographs are the ones with clear distinction between the gas and liquid phases. The use of dyed liquid enhanced visualization of phase boundaries and produced quality photographs.

6.3 PARTIAL RESULTS AND DISCUSSION

Preliminary experiments were done with q_{gas}/q_{liq} values of 1, 5, 10, 20 and single-phase runs at residual saturation. There were some important observations.

At these ratios of q_{gas}/q_{liq}, the water and gas phase travel along the plate as separate channels. These separate flow paths change with time and position. This is illustrated in the series of images in Figure 6.5, which were taken at constant gas and liquid rate. This observation implies that at these ratios, the phases move individually and not as "moving islands" or "globules" of the discontinuous phase carried along by the other phase. It also suggests that there is no local steady-state saturation.

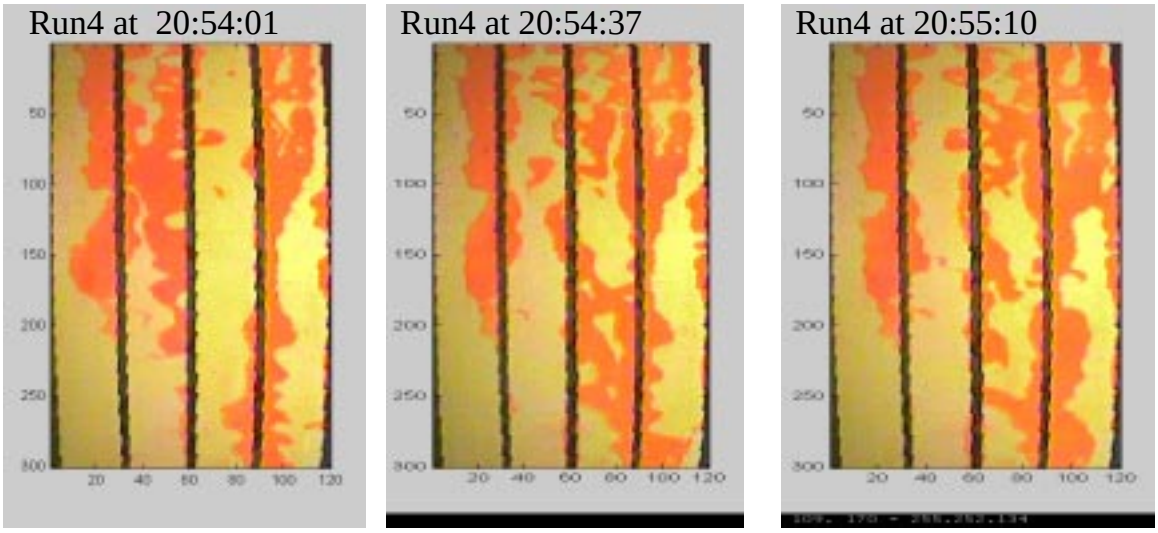

Figure 6.5: Images at constant gas and liquid rate in short time intervals to illustrate changes in the gas and liquid flow paths.

These fast changes in flow paths are accompanied by pressure fluctuations. When the gas has established enough energy to break through the water flow path, there is a corresponding increase in inlet gas pressure and decrease in water line pressure. The same is true when the water phase breaches through gas channels. This caused difficulty in obtaining pressure data from the manometers, and represents a likely source of error in pressure data.

Residual saturations obtained were very low. S_{wr} was around 0.02 - 0.06. Similarly, S_{gr} was around 0.04-0.06. This indicates that there was negligible trapping in this smooth-walled fractures.

Pan et al. (1996) discussed two approaches to data analysis: the porous medium approach where Darcy's law is used and the homogeneous single-phase approach where the system is treated as a single-phase pipe flow. Because of the observations in the experiments, it seemed appropriate to treat the data using the porous medium approach.

Darcy's law was used to obtained the single-phase and two-phase liquid permeability:

$$k_l = \frac{q_i \mu L}{(p_i - p_o)} \tag{6.1}$$

subscripts 'o' stands for outlet and 'i' for inlet, μ the viscosity, p as pressure, L for length of the plate and q as Darcy flow velocity from

$$q_o = \frac{Q_o}{bw} \tag{6.2}$$

where Q is the volumetric rate, b the aperture and w is the width of the plate.

The relative permeability is then calculated by taking the ratio of the two-phase k_l with the single-phase k_l.

The gas permeability was calculated using the equation from Scheidegger (1974):

$$k_g = 2 q_o \mu L \frac{p_o}{p_i^2 - p_o^2} \tag{6.3}$$

Similarly, taking the ratio of the two-phase k_g with single-phase run gives the relative permeability.

The complete list of calculated relative permeability values, with their corresponding saturation range is shown in Table 6.1. Figure 6.6 and 6.7 shows the plot of these data along with the X-curves. The data is clustered at small saturation range and lies far from the X-curves.

6.4 FUTURE WORK

Further experiments with nitrogen-water system will be done at higher order of variation of q_{gas}/q_{liq}. This is to obtain wider saturation range in the relative permeability values. The experiment will also be done on system with sand or glass beads in between the glass and aluminum plate to simulate flow through rough-walled fractures.

After the nitrogen-water experiments, the apparatus will be further modified for steam-water system.

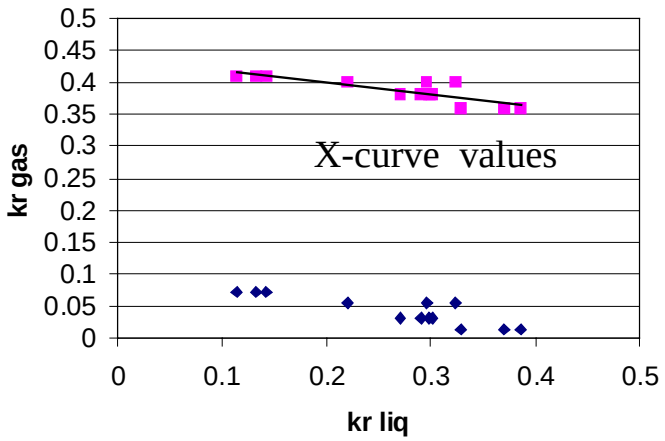

Figure 6.6: Comparison of experimental relative permeability values with X-curve values.

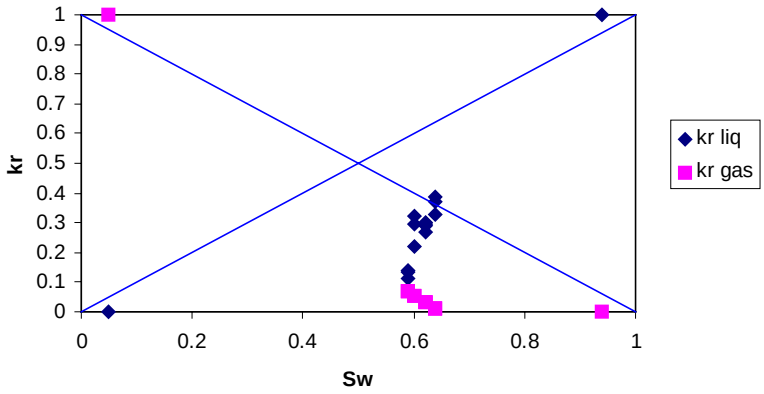

Figure 6.7: Experimental relative permeability values against saturation.

Table 6.1: Calculated Relative Permeability Values

run #	Qg	Gas Head	krg	Qw	Water Head	krl
	(cc/min)	(cm H2O)		(cc/min)	(cm H2O)	
1	74	12.5	0.013	35.16	11.5	0.385
1	74	12.5	0.013	33.77	11.5	0.370
1	74	12.5	0.013	29.97	11.5	0.328
2	172	13	0.030	26.51	11.5	0.291
2	172	13	0.030	27.45	11.5	0.301
2	172	13	0.030	27.19	11.5	0.298
3	172	13	0.030	24.71	11.5	0.271
3	332	13.7	0.055	26.98	11.5	0.296
3	332	13.7	0.055	29.51	11.5	0.323
3	332	13.7	0.055	20.04	11.5	0.220
4	407	12.8	0.072	12.36	11.0	0.142
4	407	12.8	0.072	9.92	11.0	0.114
4	407	12.8	0.072	11.52	11.0	0.132

7. INFERRING RESERVOIR CONNECTIVITY BY WAVELET ANALYSIS OF PRODUCTION DATA

This project is being conducted by Research Assistant Brian A. Arcedera and Prof. Roland Horne. The objective is to determine reservoir connectivity by applying wavelet analysis to data gathered in day-to-day operations. Use of this technique would establish the degree of connectivity between wells without doing additional tests and data gathering.

7.1 BACKGROUND

In 1998, Sullera (Sullera and Horne, 2000) used wavelet analysis and multiple regression techniques to infer injection returns by analyzing injection rates and chloride concentrations. The study indicated that wavelet analysis could isolate short-term signal variations which could be correlated from one well to another. The results of Sullera's study were verified successfully against tracer test data and qualitative field observations.

However, Sullera's study only yielded successful results in one set of field data. Other data sets analyzed did not have sufficient data points for meaningful statistical correlations. The frequency of chloride data further hindered the approach by limiting the analysis to the use of monthly data. Data with monthly frequency may not be suitable for this analysis because it does not capture the short-term variations in the signal.

7.2 INTRODUCTION

This project was conceived as an extension of Sullera's study. The study addresses the problems of lack of data and insufficient data frequency by analyzing production data (e.g. total rate, steam rate, brine rate, wellhead pressure, enthalpy). Production data is already gathered on a regular basis for normal operating records so no additional tests or data gathering needs to be done.

7.3 METHODOLOGY

The analysis required in the study can be broken into four main steps: preprocessing, wavelet analysis, cross-correlation analysis, and multiple regression analysis.

The preprocessing step rearranges the data from different sources into a uniform format for subsequent analysis. Each data set from a unique source goes through a custom translation macro which extracts the pertinent information and writes it into a new file. This uniform data format is essential in the automation of the succeeding filtration and analysis steps. The formatted data is then filtered to remove nonnumeric entries and linearly interpolated to produce data signals over a uniform time interval. Safeguards in the interpolation macro prevent interpolation over long periods of missing data. In these cases, the data signal is truncated to include only the longest relevant time period.

The processed data signal is separated into a general approximation and a series of signal fluctuations through wavelet decomposition. Wavelet analysis separates the data into small sections and fits a predetermined wavelet function to each subgroup. Each level of

wavelet decomposition handles a different section length thus capturing signal variations at different time scales. Wavelet analysis is done using the Haar wavelet (a wavelet similar to a square wave) since it best captures the fluctuations expected from the on/off variations in surface conditions. This decomposition is applied until the approximation curve becomes smooth.

The different detail signals obtained in the wavelet analysis from different wells are analyzed in groups to determine correlations between them. Different types of production data are paired and analyzed in turn (e.g. injection rate – production enthalpy, or injection rate – production wellhead pressure). For each pair of data type, cross-correlation is done for each detail level between wells to determine any signal lag so that the data can be adjusted accordingly.

The adjusted signals can now be analyzed through multiple regression to determine the effects of one data signal on another. For each pair of wells being analyzed, the different detail levels will be compared and the regression coefficients noted. The detail level with the best meaningful correlation will be analyzed further. The regression parameters obtained at the best detail level will be compared to other well pairs to infer relative connectivity strengths between them.

7.4 CONTINUING WORK

A wavelet decomposition of the monthly steam production rate of a particular well is given in Figure 7.1. The figure shows the original signal, *s*, followed by the approximation, a_5, and the different detail levels, $d_{n,}$ all plotted against the number of months elapsed. The wavelet analysis separates the general trend (declining steam production), a_5, and gives us the detail signals indicating fluctuations over different time intervals. It is these fluctuations that we hope to correlate between wells and ultimately use to determine reservoir connectivity. It is worth noting in this example that monthly data is not very suitable for our study because it may not capture short-term variations in the signal. Further, as the decomposition level goes up, the time interval we are considering increases. In Figure 7.1 for example, the detail signal at level 3, d_3, gives the signal fluctuations over a four-month period. This may be too large an interval to obtain meaningful results.

We are still at an early stage in the project and are still in the process of gathering data, setting up the macro files for handling repetitive tasks, and decomposing the data through wavelet analysis. Field data have been obtained from the MakBan and Tiwi geothermal fields in the Philippines. These data provide daily injection information as well as sporadic (approximately weekly) production data. Preformatting routines have been set up for this particular data set and we are in the process of applying wavelet decomposition on the data. The first data pairs analyzed will be injection rate against production wellhead pressure, and injection rate against production enthalpy. It is hoped that analyzing these data pairs may give more information on injection returns in the fields. In particular, information on the effects of injection returns in the form of pressure support as well as effects on reservoir enthalpy may prove useful.

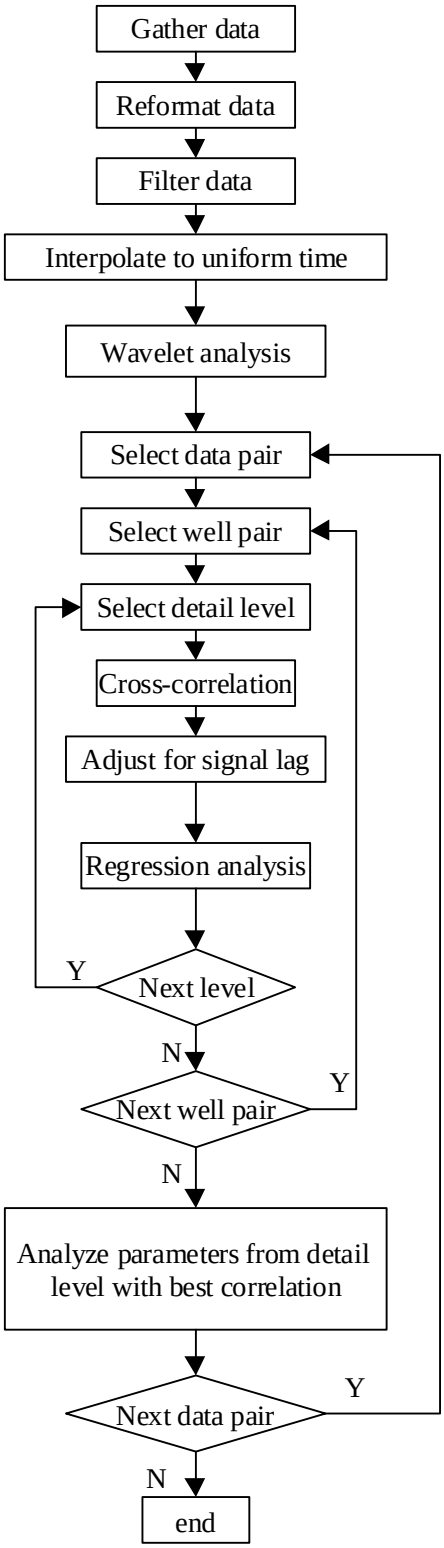

Figure 7.1: Simplified process work flow.

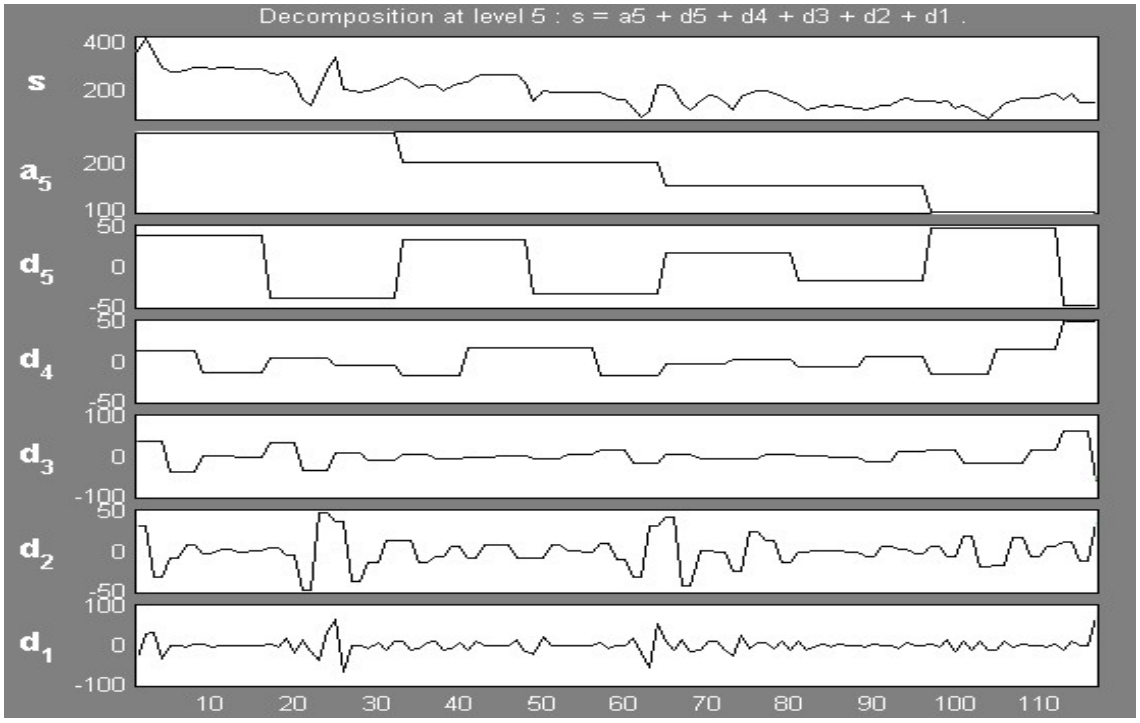

Figure 7.2: Sample wavelet decomposition of monthly steam production data.

8. REFERENCES

Aronofsky, J.S., Masse, L., and Natanson, S.G.: " A Model for the Mechanism of Oil Recovery from the Porous Matrix Due to Water Invasion in Fractured Reservoirs," *Trans*. AIME **213** (1958), 17-19.

Atkinson, P., Celati, R., Corsi, R., Kucuk, F., and Ramey, H.J., Jr.: "Thermodynamic behavior of the Bagnore geothermal field", *Geothermics*, Volume 7, (1977), 185-208.

Bourblaux, B.J. and Kalaydjian, F.J.: "Experimental Study of Cocurrent and Countercurrent Flows in Natural Porous Media," *SPERE* (1990), 361-368.

Brooks, R.H., and Corey, A.T.: "Hydraulic Properties of Porous Media," Colorado State University, Hydro paper No.5 (1964).

Goyal, K.P.: "Injection Experience in The Geysers, California – A Summary," paper presented at the 1999 GRC Annual Meeting held in Reno, NV, October 17-20, GRC *Trans*. **23**.

Grant, M.A.: "Water Content of the Kawah Kamojang Geothermal Reservoir", *Geothermics*, Volume 8, (1979), 21-30.

Grant M.A.: "Broadlands – a Gas Dominated Geothermal Field", *Geothermics*, Volume 6, (1977), 9-29.

Handy, L.L.: "Determination of Effective Capillary Pressures for Porous Media from Imbibition Data," *Trans*. AIME, Vol. 219 (1960), 75-80.

Hanselman, D. and Littlefield, B.: *Mastering Matlab 5 A Comprehensive Tutorial and Reference*, Prentice-Hall, Inc., New Jersey, 1998.

Horne, R.N.: Notes on Geothermal Reservoir Engineering, Stanford University, Stanford, California (1991).

Horne, R.N., Satik, C., Mahiya, G., Li, K., Ambusso, W., Tovar, R., Wang, C., and Nassori, H.: "Steam-Water Relative Permeability," *Proc*. of the World Geothermal Congress 2000, Kyushu-Tohoku, Japan, May 28-June 10, 2000.

Leverett, M.C.: "Capillary Behavior in Porous Solids," *Trans*., AIME, (1941), **142**, 152-168.

Li, K., and Firoozabadi, A.: "Experimental Study of Wettability Alteration to Preferential Gas-Wetness in Porous Media and its Effect," *SPEREE* (2000), 139-149.

Li, K., and Horne, R.N.: "Accurate Measurement of Steam Flow Properties," paper presented at the 1999 GRC Annual Meeting held in Reno, NV, October 17-20, GRC *Trans*. **23**.

Li, K., and Horne, R.N.: "Steam-Water Capillary Pressure in Geothermal Systems," presented at the 25th Stanford Workshop on Geothermal Reservoir Engineering, January 24-26, 2000, Stanford University, Stanford, CA 94043, USA.

Li, K., and Horne, R.N.: "Characterization of Spontaneous Water Imbibition into Gas-Saturated Rocks," SPE 62552, *Proc*. of the 2000 SPE/AAPG Western Regional Meeting held in Long Beach, California, June 19-23, 2000.

Ma, S., Morrow, N.R., and Zhang, X. (1995): "Generalized Scaling of Spontaneous Imbibition Data for Strongly Water-Wet Systems," paper 95-138, presented at the 6th Petroleum Conference of the South Saskatchewan Section, the Petroleum Society of CIM, held in Regina, Saskatchewan, Canada, October 16-18, 1995.

Mahiya, G.F.: *Experimental Measurement of Steam-Water Relative Permeability*, MS report, Stanford University, Stanford, Calif., 1999.

Moench, A., and Atkinson, P.: "Transient-Pressure Analysis in Geothermal Steam Reservoirs with an Immobile Vaporizing Liquid Phase", *Geothermics*, Volume 7, (1978), 253-264.

Melrose, J.C.: "Scaling Procedures for Capillary Pressure Data at Low Wetting-Phase Saturations, " *SPEFE*, (June. 1991), 227-232.

Melrose, J.C., Dixon, J.R., and Mallinson, J.E.: "Comparison of Different Techniques for Obtaining Capillary Pressure Data in the Low-Saturation Region, " *SPEFE*, (Sept. 1994), 185-192.

Nathenson, M.: "Some Reservoir Engineering Calculations for the Vapor Dominated System at Larderello, Italy", U.S. Geological Survey Open-file Report 75-142, April 1975.

Pan, X., Wong, R.C., and Maini, B.B.: Steady State Two-Phase Flow in a Smooth Parallel Fracture, presented at the 47th Annual Technical Meeting of the Petroleum Society in Calgary, Alberta, Canada, June 10-12, 1996.

Persoff, P., and Pruess, K.: Two-Phase Flow Visualization and Relative Permeability Measurement in Transparent Replicas of Rough-Walled Fractures, Proceedings, 16th Workshop on Geothermal Reservoir Engineering, Stanford University, Stanford, CA, Jan. 23-25, 1991, pp 203-210.

Pruess, K., and Tsang, Y.W.: On Two-Phase Relative Permeability and Capillary Pressure of Rough-Walled Rock Fractures, Water Resources Research 26 (9), (1990), pp 1915-1926.

Scheidegger, A.E. *The Physics of Flow Through Porous Media*, 3rd ed., University of Toronto, Toronto, 1974.

Sinnokrot, A.A: The Effect of Temperature on Oil-Water Capillary Pressure Curves of Limestones and Sandstones, Ph.D. dissertation, Stanford University, Stanford, CA, USA (1969).

Sullera, M.M., and Horne, R.N.: "Inferring Injection Returns from Chloride Monitoring Data", to appear in *Geothermics*, 2000.

Udell, K.S.: "The Thermodynamics of Evaporation and Condensation in Porous Media," paper SPE 10779, presented at the 1982 SPE California Regional Meeting, San Francisco, CA, USA, March 24-26, 1982.

Ward, J.S., and Morrow, N.R.: "Capillary Pressures and Gas Relative Permeabilities of Low-Permeability Sandstone," *SPEFE*, (Sept. 1987), 345-356.

Schembre, J.M., Akin, S., Castanier, L.M., and Kovscek, A.R.: “Spontaneous Water Imbibition into Diatomite,” paper SPE 46211, presented at the 1998 Western Region Meeting, Bakersfield, California, May 10-13.

Schechter, D.S. and Guo, B.: “An Integrated Investigation for Design of a CO_2 Pilot in the Naturally Fractured Spraberry Trend Area, West Texas,” paper SPE 39881, presented at the 1998 SPE International Petroleum Conference and Exhibition held in Villahermosa, Mexico, March 3-5, 1998.

Zhang, X., Morrow, N.R., and Ma, S.: “Experimental Verification of a Modified Scaling Group for Spontaneous Imbibition,” *SPERE*, November (1996), 280-285.